

Uncertainty quantification in Discrete Fracture Network models: stochastic fracture transmissivity

Original

Uncertainty quantification in Discrete Fracture Network models: stochastic fracture transmissivity / Berrone, Stefano; Canuto, Claudio; Pieraccini, Sandra; Scialo', Stefano. - In: COMPUTERS & MATHEMATICS WITH APPLICATIONS. - ISSN 0898-1221. - STAMPA. - 70:4(2015), pp. 603-623. [[10.1016/j.camwa.2015.05.013](https://doi.org/10.1016/j.camwa.2015.05.013)]

Availability:

This version is available at: 11583/2564948 since: 2016-10-26T16:45:19Z

Publisher:

Elsevier

Published

DOI:[10.1016/j.camwa.2015.05.013](https://doi.org/10.1016/j.camwa.2015.05.013)

Terms of use:

This article is made available under terms and conditions as specified in the corresponding bibliographic description in the repository

Publisher copyright

(Article begins on next page)

Uncertainty quantification in Discrete Fracture Network models: stochastic fracture transmissivity

S. Berrone, C. Canuto, S. Pieraccini and S. Scialò

*Dipartimento di Scienze Matematiche, Politecnico di Torino,
Corso Duca degli Abruzzi 24, 10129 Torino, Italy*

`{stefano.berrone, claudio.canuto, sandra.pieraccini, stefano.scialo}@polito.it`

Abstract

We consider flows in fractured media, described by Discrete Fracture Network (DFN) models. We perform an Uncertainty Quantification analysis, assuming the fractures' transmissivity coefficients to be random variables. Two probability distributions (log-uniform and log-normal) are used within different laws that express the coefficients in terms of a family of independent stochastic variables; truncated Karhunen-Loève expansions provide instances of such laws.

The approximate computation of quantities of interest, such as mean value and variance for outgoing fluxes, is based on a stochastic collocation approach that uses suitable sparse grids in the range of the stochastic variables (whose number defines the stochastic dimension of the problem). This produces a non-intrusive computational method, in which the DFN flow solver is applied as a black-box. A very fast error decay, related to the analytical dependence of the observed quantities upon the stochastic variables, is obtained in the low dimensional cases using isotropic sparse grids; comparisons with Monte Carlo results show a clear gain in efficiency for the proposed method. For increasing dimensions attained via successive truncations of Karhunen-Loève expansions, results are still good although the rates of convergence are progressively reduced. Resorting to suitably tuned anisotropic grids is an effective way to contrast such curse of dimensionality: in the explored range of dimensions, the resulting convergence histories are nearly independent of the dimension.

Keywords: Fracture networks, Darcy's law in fractured media, Uncertainty quantification, Stochastic collocation methods, Sparse grids

2010 MSC: 65C20, 65N35, 86-08

1. Introduction

Efficient simulation and investigation of subsurface flow is an up-to-date open research topic. The complexity of the problem and the increasing interest of many applications (analysis of pollutant diffusion in aquifers, Oil&Gas enhanced production, nuclear waste geological storage, carbon dioxide geological storage, geothermal applications, energy and gas storage...) make this research issue of great interest. In these applications, the computational domain for the simulations consists of underground geological reservoirs, that usually have huge complex heterogeneous structure and for which only stochastic data are typically available.

Among the models proposed in literature for the simulation of flows in fractured media, we consider here the Discrete Fracture Network (DFN) model [1].

A DFN model describes a geological reservoir as a system of intersecting planar polygons representing the network of fractures in the underground. Fracture intersections are called *traces*. In the present work we consider impervious surrounding rock matrix, so that no flux exchange occurs with the surrounding medium. The quantity of interest is the flow potential, called hydraulic head, given by the sum of pressure and elevation. The hydraulic head is ruled by Darcy’s law in each fracture, with additional matching conditions which ensure hydraulic head continuity and flux balance at fracture intersections. Thanks to these matching conditions, the hydraulic head is continuous across traces but jumps of gradients may occur as a consequence of flux exchange between intersecting fractures. Hence, traces are typically interfaces of discontinuities for the gradient of the solution.

Standard finite element methods or mixed finite elements are widely used for obtaining a numerical solution also in this context, but they require mesh elements to conform with the traces in order to correctly describe the irregular behavior of the solution. This poses a severe limitation, since realistic fracture networks are typically very intricate, with fractures intersecting each other with arbitrary orientation, position, density and dimension. A conforming meshing process may result infeasible, or might generate a poor quality mesh, since a coupled meshing process on all the fractures of the system may lead to elongated elements.

In [2, 3, 4] the authors propose a PDE-constrained optimization approach to flow simulations on arbitrary DFNs, in which neither fracture/fracture nor fracture/trace mesh conformity is required. The method is based on the minimization of a quadratic functional constrained by the state equations describing the flow on the fractures. The approach totally circumvents the problem of mesh generation, without any need of geometrical modification tailored on the DFN (e.g., fracture or trace removal or displacement). The method has proven to be quite robust on several medium size DFNs [5, 6]. Extended Finite Elements (XFEM) [7, 8, 9] are used in order to enrich the numerical solution and correctly reproduce irregularities in the solution. For a list of references to other numerical approaches for DFN flow simulations see, e.g., [2, 5].

Coming to the topic of the present paper, we observe that since the actual layout of fractures in a large scale geological basin cannot be precisely established in a deterministic way, DFNs are usually built as representations of natural media starting from stochastic distributions derived from “in situ” measurements [1, 10]. Obtaining some accurate quantification of the influence of these distributions on the outputs of DFN models is therefore of paramount importance to assess the reliability of the simulation process. Modern techniques of Uncertainty Quantification for PDE-based models allow us to combine accuracy with computational efficiency, a mandatory requirement for our application, where the cost of each single DFN simulation may be by far non-negligible. This motivates our interest in applying UQ techniques, and in particular stochastic collocation methods, to flow simulation in fractured media.

The paper is organized as follows. In Sect. 2 we describe the DFN model and its numerical discretization. In Sect. 3 we recall the basic concepts of Uncertainty Quantification that will be used in our analysis, and we establish conditions assuring the analytical dependence of the solution upon the chosen set of independent stochastic variables. Sect. 4 is devoted to the description of some representative DFNs on which we specify the boundary value problem, assuming randomness in the transmissivity coefficients; the results of some numerical tests are illustrated. Finally, in Sect. 5 we consider certain Karhunen-Loève (truncated) expansions of the transmissivity coefficients, and we study the effect of increasing the stochastic dimensionality.

2. Model description and numerical discretization

Let us consider a DFN \mathcal{D} given by the union of open planar polygonal sets F_i , with $i = 1, \dots, I$, called fractures; let us denote by ∂F_i the boundary of F_i and by $\partial \mathcal{D} = \cup_{i=1}^I \partial F_i$ the union of all fracture boundaries. We decompose the latter set as $\partial \mathcal{D} = \Gamma_D \cup \Gamma_N$ with $\Gamma_D \cap \Gamma_N = \emptyset$, $\Gamma_D \neq \emptyset$ being Γ_D the Dirichlet boundary and Γ_N the Neumann boundary. Similarly, the boundary of each fracture is divided in a Dirichlet part $\Gamma_{iD} = \Gamma_D \cap \partial F_i$ and a Neumann part $\Gamma_{iN} = \Gamma_N \cap \partial F_i$, hence $\partial F_i = \Gamma_{iD} \cup \Gamma_{iN}$, with $\Gamma_{iD} \cap \Gamma_{iN} = \emptyset$. For the ease of description we also assume that $\Gamma_{iD} \neq \emptyset$ for all $i = 1, \dots, I$; this rather strong assumption can be actually relaxed, see Remark 2.1 below.

Boundary data $H_i^D \in H^{\frac{1}{2}}(\Gamma_{iD})$ and $G_i^N \in H^{-\frac{1}{2}}(\Gamma_{iN})$ are given and define the Dirichlet and Neumann boundary conditions, respectively, on the boundary ∂F_i . Fractures have arbitrary orientations in space, so \mathcal{D} is a two-dimensional manifold contained in \mathbb{R}^3 . Traces are denoted by S_m , $m = 1, \dots, M^T$; \mathcal{S} denotes the set of all the traces of the system, and \mathcal{S}_i , for $i = 1, \dots, I$, denotes the subset of \mathcal{S} corresponding to the traces belonging to F_i . We assume that each S_m uniquely identifies a couple of indices $I_{S_m} = \{i, j\}$, such that $S_m \subseteq \bar{F}_i \cap \bar{F}_j$.

According to Darcy's law, the hydraulic head H in \mathcal{D} is determined by a system of equations on each fracture, defined as follows. For the sake of simplicity of notation, in this section we assume that traces are non-intersecting, but we remark that the numerical method described in the following is not affected by this assumption. Let H_i denote the restriction of the solution H to fracture F_i and let \mathbf{K}_i be a symmetric and uniformly positive-definite tensor (the fracture transmissivity). Let us introduce for each fracture the following functional spaces:

$$V_i = H_{0,D}^1(F_i) = \left\{ v \in H^1(F_i) : v|_{\Gamma_{iD}} = 0 \right\},$$

and

$$V_i^D = H_D^1(F_i) = \left\{ v \in H^1(F_i) : v|_{\Gamma_{iD}} = H_i^D \right\}.$$

Then H_i satisfies, for $i = 1, \dots, I$, the following problem: find $H_i \in V_i^D$ such that for all $v \in V_i$

$$\int_{F_i} \mathbf{K}_i \nabla H_i \cdot \nabla v = \int_{F_i} q_i v + \langle G_i^N, v|_{\Gamma_{iN}} \rangle_{H^{-\frac{1}{2}}(\Gamma_{iN}), H^{\frac{1}{2}}(\Gamma_{iN})} + \sum_{S \in \mathcal{S}_i} \left\langle \left[\frac{\partial H_i}{\partial \hat{\nu}_S^i} \right]_S, v|_S \right\rangle_{H^{-\frac{1}{2}}(S), H^{\frac{1}{2}}(S)} \quad (2.1)$$

where $q_i \in L^2(F_i)$ is a source term on F_i , the symbol $\frac{\partial H_i}{\partial \hat{\nu}^i}$ represents the outward co-normal derivative of the hydraulic head,

$$\frac{\partial H_i}{\partial \hat{\nu}^i} = \hat{\mathbf{n}}_i^T \mathbf{K}_i \nabla H_i$$

with $\hat{\mathbf{n}}_i$ outward normal to the boundary Γ_{iN} , and $\left[\frac{\partial H_i}{\partial \hat{\nu}_S^i} \right]_S$ denotes the jump of the co-normal derivative along the unique normal $\hat{\mathbf{n}}_S^i$ to the trace S on F_i , and represents the flux incoming into the fracture F_i through the trace S .

Equations (2.1) for $i = 1, \dots, I$ are coupled with the following additional matching conditions imposing hydraulic head continuity and flux balance across the traces:

$$H_i|_{S_m} - H_j|_{S_m} = 0, \quad \text{for } i, j \in I_{S_m}, \quad \forall m = 1, \dots, M^T, \quad (2.2)$$

$$\left[\frac{\partial H_i}{\partial \hat{\nu}_{S_m}^i} \right]_{S_m} + \left[\frac{\partial H_j}{\partial \hat{\nu}_{S_m}^j} \right]_{S_m} = 0, \quad \text{for } i, j \in I_{S_m}, \quad \forall m = 1, \dots, M^T. \quad (2.3)$$

Following the method described in [2, 3, 4], instead of solving the coupled system of equations (2.1)-(2.3), the solution is obtained by solving a PDE-constrained optimization problem. More precisely, for each trace S in each fracture F_i , let us introduce the control variables $U_i^S \in \mathcal{U}^S := H^{-\frac{1}{2}}(S)$, defined as $U_i^S = \left[\left[\frac{\partial H_i}{\partial \nu_S^+} \right] \right]_S$. Equation (2.1), prescribed on the fractures, can be equivalently restated as:

$$\int_{F_i} \mathbf{K}_i \nabla H_i \cdot \nabla v = \int_{F_i} q_i v + \langle G_i^N, v|_{\Gamma_{iN}} \rangle_{H^{-\frac{1}{2}}(\Gamma_{iN}), H^{\frac{1}{2}}(\Gamma_{iN})} + \sum_{S \in \mathcal{S}_i} \langle U_i^S, v|_S \rangle_{\mathcal{U}^S, \mathcal{U}^{S'}}. \quad (2.4)$$

Let us define $\mathcal{U}^{\mathcal{S}_i} = H^{-\frac{1}{2}}(\mathcal{S}_i)$ and let $U_i \in \mathcal{U}^{\mathcal{S}_i}$ be the tuple of control variables U_i^S for $S \in \mathcal{S}_i$. Analogously, let $U \in \mathcal{U}^{\mathcal{S}}$ denote the tuple of control variables U_i for $i = 1, \dots, I$. Furthermore, let \mathcal{R}_i denote a linear operator providing a continuous lifting of the Dirichlet boundary conditions on Γ_{iD} to F_i . Let us introduce the following linear bounded operators:

$$\begin{aligned} A_i &\in \mathcal{L}(H^1(F_i), V_i'), & \langle A_i w, v \rangle_{V_i', V_i} &= (\mathbf{K}_i \nabla w, \nabla v)_{L^2(F_i)} \\ B_i^S &\in \mathcal{L}(\mathcal{U}^S, V_i'), & \langle B_i^S U_i^S, v \rangle_{V_i', V_i} &= \langle U_i^S, v|_S \rangle_{\mathcal{U}^S, \mathcal{U}^{S'}}, \\ B_i &= \prod_{S \in \mathcal{S}_i} B_i^S \in \mathcal{L}(\mathcal{U}^{\mathcal{S}_i}, V_i'), & \langle B_i U_i, v \rangle_{V_i', V_i} &= \langle U_i, v|_{\mathcal{S}_i} \rangle_{\mathcal{U}^{\mathcal{S}_i}, \mathcal{U}^{\mathcal{S}_i'}}, \end{aligned} \quad (2.5)$$

with $w \in H^1(F_i)$ and $v \in V_i$. The operator $B_{iN} \in \mathcal{L}(H^{-\frac{1}{2}}(\Gamma_{iN}), V_i')$ imposing Neumann boundary conditions is defined by the conditions

$$\langle B_{iN} G_i^N, v \rangle_{V_i', V_i} = \langle G_i^N, v|_{\Gamma_{iN}} \rangle_{H^{-\frac{1}{2}}(\Gamma_{iN}), H^{\frac{1}{2}}(\Gamma_{iN})}, \quad \forall v \in V_i.$$

With these definitions at hand, problems (2.4) are rewritten as: $\forall i = 1, \dots, I$, find $H_i \in V_i^D$, with $H_i = H_i^0 + \mathcal{R}_i H_i^D$ and $H_i^0 \in V_i$, such that

$$A_i H_i^0 = q_i + B_i U_i + B_{iN} G_i^N - A_i^D H_i^D \quad \text{in } V_i', \quad (2.6)$$

with $A_i^D = A_i \mathcal{R}_i \in \mathcal{L}(H^{\frac{1}{2}}(\Gamma_{iD}), V_i')$. We remark that, for a given U_i , the solution H_i to (2.6) exists and is unique for a non-isolated fracture.

Now let us introduce the functional

$$J(H, U) = \frac{1}{2} \sum_{m=1}^{M^T} \left(\|H_i|_{S_m} - H_j|_{S_m}\|_{H^{\frac{1}{2}}(S_m)}^2 + \|U_i^{S_m} + U_j^{S_m}\|_{H^{-\frac{1}{2}}(S_m)}^2 \right), \quad (2.7)$$

with $i, j \in I_{S_m}$, $i \neq j$. The functional J is quadratic and, as shown in [2], its unique minimum is obtained for values of H and of the control functions U that correspond to the fulfilment of conditions (2.2) and (2.3) on the traces. In other words, the solution of the problem

$$\min J(H, U) \quad \text{subject to (2.6)} \quad (2.8)$$

corresponds to the solution of the coupled system of equations (2.1)-(2.3).

Remark 2.1. The assumption $\Gamma_{iD} \neq \emptyset$ for all $i = 1, \dots, I$ can be removed by defining the control variable as $U_i^S = \alpha H_i|_S + \left[\left[\frac{\partial H_i}{\partial \nu_S^+} \right] \right]_S$. In this case equation (2.4) and correspondingly operator A_i in (2.5), and functional J in (2.7) have to be modified accordingly, see [4]. With these modifications the solution to (2.6) exists and is unique for a non-isolated fracture F_i even if we set Neumann boundary conditions on the whole ∂F_i . In this section we consider, for the ease of description, the simplified model recalled above. Nevertheless, the modified model has been used for obtaining the numerical results reported in Section 4 and Section 5.

The model described so far allows, on each fracture, for a tensor transmissivity depending on the position. For the sake of simplicity, in the following we assume that the transmissivity is given by a constant scalar value K_i on each fracture F_i .

2.1. Discretization and solution

Let us now briefly introduce the discrete formulation of the constrained minimization problem (2.8). To this end, a finite dimensional space on each fracture is chosen. Since the solution displays a non-smooth behavior across traces, a special care is devoted to reproducing such an irregular behavior. Two approaches have been considered: the first one consists in using extended finite elements (XFEM), as in [2, 3, 4], allowing for totally non-conforming meshes. The XFEM allows the description of irregular solutions regardless of the position of mesh elements with respect to the irregularity interfaces, so that the numerical triangulation for DFN simulations can be generated independently on each fracture, without any kind of conformity constraint along the traces, thus circumventing any problem related to mesh generation. The second approach consists in using the virtual element method (VEM) [11, 12] allowing for a partial mesh non-conformity, yet guaranteeing an independent meshing process on each fracture, as done in [5]. The description which follows does not rely on the particular choice of finite element spaces.

Let us introduce such a space on each fracture F_i , with dimension N_i , and a corresponding Lagrangian basis $(\phi_{i,1}, \dots, \phi_{i,k}, \dots, \phi_{i,N_i})$, such that $h_i = \sum_{k=1}^{N_i} h_{i,k} \phi_{i,k}$ is the finite dimensional approximation of the hydraulic head H_i . Overloading the notation, h_i will also denote the vector of the N_i coefficients $(h_{i,1}, \dots, h_{i,N_i})^T$. Similarly, we introduce a finite dimensional space for each trace S_m on each fracture F_i , with dimension N_m^i , and a Lagrangian basis $(\psi_{m,1}^i, \dots, \psi_{m,k}^i, \dots, \psi_{m,N_m^i}^i)$ for this space; thus, we write the approximation of the control function $U_i^{S_m}$ as $u_m^i = \sum_{k=1}^{N_m^i} u_{m,k}^i \psi_{m,k}^i$, again overloading the same notation for the vector of coefficients $(u_{m,1}^i, \dots, u_{m,N_m^i}^i)^T$. Let us further define the discrete version of the cost functional J , obtained replacing the $H^{\frac{1}{2}}(S)$ - and $H^{-\frac{1}{2}}(S)$ -norms with weighted L^2 -norms of the traces, thus yielding:

$$J(h, u) = \frac{1}{2} \sum_{m=1}^{M^T} \left(\eta_h \int_{S_m} \left(\sum_{k=1}^{N_i} h_{i,k} \varphi_{i,k}|_{S_m} - \sum_{k=1}^{N_j} h_{j,k} \varphi_{j,k}|_{S_m} \right)^2 + \eta_u \int_{S_m} \left(\sum_{k=1}^{N_m^i} u_{m,k}^i \psi_{m,k}^i + \sum_{k=1}^{N_m^j} u_{m,k}^j \psi_{m,k}^j \right)^2 \right), \quad (2.9)$$

again with $i, j \in I_{S_m}$, $i \neq j$. The algebraic form of the functional is then

$$J(h, u) := \frac{1}{2} h^T G^h h + \frac{1}{2} u^T G^u u, \quad (2.10)$$

where, denoting by $N^F = \sum_{i=1}^I N_i$ the total number of DOFs on the fractures for the state variable and by $N^T = \sum_{i=1}^I \sum_{m \in S_i} N_m^i$ the total number of DOFs on the traces for the control variables, $G^h \in \mathbb{R}^{N^F \times N^F}$, $G^u \in \mathbb{R}^{N^T \times N^T}$ are symmetric and positive-semidefinite sparse matrices, whereas $h \in \mathbb{R}^{N^F}$ and $u \in \mathbb{R}^{N^T}$ are vectors collecting all DOFs for the hydraulic head on fractures and for the control variable on traces, respectively. The definition of the previous matrices also accounts for the weighting factors. The constraints are written as

$$Ah - \mathcal{B}u = q, \quad (2.11)$$

where $A \in \mathbb{R}^{N^F \times N^F}$ is a block-diagonal positive-definite matrix and $\mathcal{B} \in \mathbb{R}^{N^F \times N^T}$ is a sparse matrix, obtained by assembling the discrete counterparts of the operators A_i and B_i in (2.6), respectively, on all fractures. The vector $q \in \mathbb{R}^{N^F}$ accounts for possible source terms and boundary conditions. The problem under consideration is therefore an equality-constrained quadratic programming problem, defined as

$$\min J(h, u) \quad \text{subject to (2.11).} \quad (2.12)$$

Exploiting the linearity of the constraints (2.11), it is possible to formally derive an equivalent unconstrained minimization problem:

$$\begin{aligned} \min \hat{J}(u) &:= \frac{1}{2} u^T (\mathcal{B}^T A^{-T} G^h A^{-1} \mathcal{B} + G^u) u + q^T A^{-T} G^h A^{-1} \mathcal{B} u \\ &=: \frac{1}{2} u^T \hat{G} u + \hat{q}^T u. \end{aligned}$$

With this formulation, a gradient based method can be efficiently used to solve the problem. Indeed, the core of the method, i.e., the repeated evaluation of the gradient of J , can be split over the various fractures, allowing for parallel computations [6].

The first-order optimality conditions for problem (2.12) are expressed as follows:

$$\begin{pmatrix} G^h & 0 & A^T \\ 0 & G^u & -\mathcal{B}^T \\ A & -\mathcal{B} & 0 \end{pmatrix} \begin{pmatrix} h \\ u \\ -p \end{pmatrix} = \begin{pmatrix} 0 \\ 0 \\ q \end{pmatrix}, \quad (2.13)$$

where p denotes the vector of Lagrange multipliers. It is proven in [2] that the matrix defining the saddle-point problem (2.13) is nonsingular.

3. The uncertainty quantification setting

The exact or discretized DFN models discussed so far are all deterministic: we assume to have full knowledge of the data of our problem (the geometric parameters defining the network configuration \mathcal{D} , the transmissivity tensors \mathbf{K}_i , the boundary data H_i^D and G_i^D , and the source terms q_i) and correspondingly we obtain the exact solution (H, U) , or the discrete solution (h, u) for a given discretization of \mathcal{D} . In the sequel, we denote by \mathfrak{d} the set of data, which we assume to vary in some normed space Z , and by $\mathfrak{s} = \mathfrak{s}(\mathfrak{d})$ the corresponding (exact or discrete) solution, which belongs to some normed space W .

This scenario is far from being realistic, due to the enormous uncertainty that in practice affects our knowledge of data. Hence, it appears wiser to adopt a probabilistic approach, i.e., to see the data (or at least part of them) as random variables, endowed with a certain known (or guessed) probability distribution, and obtain the solution from the DFN model as a dependent random variable, of which we compute suitable statistics in order to rigorously quantify the amount of uncertainty affecting it.

To be more precise, let $(\Omega, \mathcal{F}, \mathbb{P})$ denote a complete probability space, where Ω is the set of outcomes, \mathcal{F} its σ -algebra, and $\mathbb{P} : \Omega \rightarrow [0, 1]$ the probability measure. We assume that $\mathfrak{d} : \Omega \rightarrow Z$ is a given random field, describing the data of our problem; then, assuming the continuity of the solution mapping $\mathfrak{d} \mapsto \mathfrak{s}$ from Z to W , the Doob-Dynkin Lemma guarantees that the solution $\mathfrak{s} : \Omega \rightarrow W$, $\mathfrak{s}(\omega) := \mathfrak{s}(\mathfrak{d}(\omega))$ almost surely (a.s.) in Ω , is itself a random field. Consequently, if a continuous mapping $Q : W \rightarrow \mathbb{R}$ defines a “quantity of interest” $Q(\mathfrak{s})$

attached to the solution \mathfrak{s} , then $Q : \Omega \rightarrow \mathbb{R}$, $Q(\omega) = Q(\mathfrak{s}(\omega))$ a.s. in Ω , is a random variable, for which we can compute, e.g., mean value (expectation) and variance

$$\mathbb{E}(Q) = \int_{\Omega} Q(\omega) \, d\mathbb{P}, \quad \sigma^2(Q) = \mathbb{E}(Q^2) - \mathbb{E}(Q)^2,$$

provided Q has bounded second-order moment (i.e., $Q \in L^2(\Omega, d\mathbb{P})$).

A fairly common assumption, that may allow us to treat the stochastic problem defined above by purely deterministic computations, consists in requiring that the data \mathfrak{d} depends on ω via a number of elementary independent random variables $Y_1(\omega), Y_2(\omega), \dots$, each one taking values in a interval of the real line; thus, we write $\mathfrak{d}(\omega) = \hat{\mathfrak{d}}(Y_1(\omega), Y_2(\omega), \dots)$. This is the situation encountered, e.g., when one resorts to the Karhunen-Loève expansion of a Gaussian variable [13]; other popular cases involve Wiener's polynomial chaos expansions and their generalizations [14], Fourier expansions [15], and so on. The number of elementary variables $Y_n(\omega)$ may be infinite, but we always assume that only a finite number of them, say the first N , are relevant in the description of data randomness, and we neglect the others. Thus, we have

$$\mathfrak{d}(\omega) = \hat{\mathfrak{d}}(Y_1(\omega), Y_2(\omega), \dots, Y_N(\omega)) \quad (3.1)$$

and we call N the stochastic dimension of our problem. We also assume that the variables Y_n are identically distributed, with images $y_n = Y_n(\omega)$ ranging in an interval \mathcal{Y} of the real line, and that they are absolutely continuous with respect to a density function $\rho : \mathcal{Y} \rightarrow [0, \infty)$.

As a consequence of these assumptions, data randomness will be expressed by (3.1), where the function $\hat{\mathfrak{d}}(y_1, y_2, \dots, y_N)$ on the right-hand side is defined in \mathcal{Y}^N with values in Z . Since the solution \mathfrak{s} and the quantity of interest Q depend on \mathfrak{d} , their randomness, too, can be expressed in terms of y_1, y_2, \dots, y_N as

$$\begin{aligned} \mathfrak{s}(\omega) &= \hat{\mathfrak{s}}(Y_1(\omega), Y_2(\omega), \dots, Y_N(\omega)), & \text{with } \hat{\mathfrak{s}} : \mathcal{Y}^N &\rightarrow W, \\ Q(\omega) &= \hat{Q}(Y_1(\omega), Y_2(\omega), \dots, Y_N(\omega)), & \text{with } \hat{Q} : \mathcal{Y}^N &\rightarrow \mathbb{R}. \end{aligned}$$

Furthermore, setting $\mathbf{y} = (y_1, y_2, \dots, y_N)$, $\varrho(\mathbf{y}) = \rho(y_1)\rho(y_2)\cdots\rho(y_N)$ and $d\mathbf{y} = dy_1 dy_2 \cdots dy_N$, we have

$$\mathbb{E}(Q) = \int_{\mathcal{Y}^N} \hat{Q}(\mathbf{y}) \varrho(\mathbf{y}) d\mathbf{y}$$

and similarly for $\sigma^2(Q)$. For the sake of simplicity, from now on we drop the hat symbol and we write $\mathfrak{s} = \mathfrak{s}(\mathbf{y})$, $Q = Q(\mathbf{y})$ and so on.

3.1. Approximation

In order to efficiently compute accurate approximations of the function \mathfrak{s} or of derived quantities such as $\mathbb{E}(Q)$, one can exploit the rich methodology developed in the two last decades, and particularly in more recent years, for PDE-based uncertainty quantification. Stochastic Galerkin methods (see, e.g., [16, 14, 17]) and stochastic collocation methods (see, e.g., [18, 19, 20]) are among the major families of methods, built on different approaches: in the former family, the approximate solution is sought as a Galerkin projection upon a finite dimensional space depending on both physical and stochastic variables, whereas in the latter family the approximation is built by interpolating the exact solution with respect to the stochastic variables at a deterministically chosen set of points in \mathcal{Y}^N . While the Galerkin approach may have some theoretical advantages, its use is confined to special classes of problems, since it requires a significant modification of

the solver associated with the physical model (the DFN model in our case). On the contrary, the collocation approach suffers only in marginal situations of a loss of accuracy with respect to a Galerkin approach, yet it allows a *non-intrusive* implementation in which the deterministic solver is used as a black-box: precisely, the model equations are solved several times in a fully independent manner with different input data defined by points in \mathcal{Y}^N (the collocation points), then the outputs are combined to form the interpolant of the exact solution. The stochastic collocation approach is a *must* in our application, due to the complexity of the model which is reflected by a high computational cost of each realization. Therefore, we now focus on the main implementation aspects of this approach.

3.1.1. Sparse grids

Clever strategies for selecting the set of collocation points in \mathcal{Y}^N are fundamental for the efficiency, and even the feasibility, of a stochastic collocation method. Since \mathcal{Y}^N is the Cartesian product of N copies of an interval of the real line, it is natural to start with a grid in \mathcal{Y} that guarantees accurate univariate interpolation/quadrature results. However, the relevant stochastic dimension N may be very large (often in the order of tens or even hundreds), which precludes the naive tensorization of 1D grids to get full Cartesian grids in \mathcal{Y}^N , as the number of collocation points would soon become prohibitive as N increases.

A popular remedy is to resort to *sparse grids* [21, 22], in which only particular subsets of tensorial grids are activated. Hereafter we introduce the constitutive ingredients of Smolyak's sparse-grid method. Since our main interest will be the computation of integral quantities such as $\mathbb{E}(Q)$ and $\sigma^2(Q)$, we adopt the terminology of sparse-grid quadratures. Indeed, we assume we want to approximate the integral

$$\text{Int}(\Phi) = \int_{\mathcal{Y}^N} \Phi(\mathbf{y}) \varrho(\mathbf{y}) d\mathbf{y}$$

of a continuous, ϱ -integrable function defined in \mathcal{Y}^N .

- i) For each integer $i \geq 0$, we choose a univariate quadrature formula in \mathcal{Y} for the measure $\rho(y)dy$ using $m(i)$ quadrature points; let $\text{Int}(\varphi; m(i))$ denote the corresponding approximation of the integral $\text{Int}(\varphi) = \int_{\mathcal{Y}} \varphi(y) \rho(y) dy$. We call i the *level* of the quadrature formula. We assume that the sequence $m(i)$ is strictly increasing.
- ii) For $i = 0$, we set $\Delta(\varphi; m(0)) = \text{Int}(\varphi; m(0))$. For $i > 0$, we define the *detail* $\Delta(\varphi; m(i)) = \text{Int}(\varphi; m(i)) - \text{Int}(\varphi; m(i-1))$.
- iii) For a multi-index $\mathbf{i} = (i_1, i_2, \dots, i_N) \in \mathbb{N}^N$, we define the *hierarchical surplus*

$$\Delta(\Phi; m(\mathbf{i})) = \bigotimes_{n=1}^N \Delta(\Phi; m(i_n)) .$$

- iv) Given a finite set $\mathcal{I} \subset \mathbb{N}^N$ of multi-indices, we define the corresponding sparse-grid approximation of $\text{Int}(\Phi)$ as

$$\text{Int}(\Phi; \mathcal{I}) = \sum_{\mathbf{i} \in \mathcal{I}} \Delta(\Phi; m(\mathbf{i})) . \quad (3.2)$$

Usually, one requires the admissibility of the set \mathcal{I} , i.e., the property that $\mathbf{i} \in \mathcal{I}$ implies $\mathbf{i} - \mathbf{e}_n \in \mathcal{I}$ for all $i_n > 0$, $1 \leq n \leq N$, where \mathbf{e}_n denotes the n -th vector of the canonical basis in \mathbb{N}^N .

Concerning the choice of the sequence of univariate quadratic formulas, the cost of each call to the DFN solver suggests to look for high-precision nested grids, in order to re-use expensive information from previous levels. For the uniform probability density, we resort to Gauss-Patterson formulas [23] (Clenshaw-Curtis formulas [24] could be an alternative). For the normal probability density, we use Kronrod-Patterson-Normal formulas [25]. More details on the chosen formulas are given in Sect. 4.

The index set \mathcal{I} will be chosen within a parametrized family $\mathcal{I}(w)$. For instance, total-degree *isotropic* grids are defined by setting

$$\mathcal{I}(w) = \{\mathbf{i} \in \mathbb{N}^N : \sum_{n=1}^N i_n \leq w\} . \quad (3.3)$$

This choice may soon become unfeasible if the stochastic dimension is not small, as the cardinality of $\mathcal{I}(p)$ grows too fastly with p ; furthermore, the rate of decay of the approximation error versus the cardinality of $\mathcal{I}(p)$ gets worser and worser as N increases (the so-called curse of dimensionality). A possible remedy is to exploit some knowledge about the dependence of the solution upon each stochastic variable y_n , and introduce *anisotropic grids* [26], defined by index sets of the form

$$\mathcal{I}(w; \boldsymbol{\beta}) = \{\mathbf{i} \in \mathbb{N}^N : \sum_{n=1}^N \beta_n i_n \leq w\} , \quad (3.4)$$

where $\boldsymbol{\beta}$ is a vector of suitably designed positive weights. In this way, lower quadrature levels are activated in the less important stochastic directions. A more drastic remedy consists in choosing the index set in an *adaptive* manner [27], by looking at those hierarchical surpluses that provide the higher profits. Their selection is based on some reliable estimate of the error reduction produced by including each surplus in the sum (3.2), normalized by the cost of computing it. For a related approach, see also [28].

In the present paper, we will employ both isotropic and anisotropic sparse grids, deferring to a forthcoming work the analysis of the performance of adaptive grids for our application.

3.2. The smoothness of the solution with respect to the stochastic variables

Hereafter, we investigate the dependence of the solution upon the stochastic variables, assuming that the transmissivity coefficients are the only sources of randomness. Randomness in the boundary conditions or the source term is easier to study, as the solution depends linearly on such data. On the contrary, randomness in the network geometry requires a more careful and delicate analysis, since traces may suddenly appear or disappear while varying the stochastic parameters they depend upon; for this reason, we will devote a specific forthcoming paper to investigate this situation.

Randomness in the operator coefficients, e.g., for modelling heat transfer or flows in porous media, has been thoroughly studied in recent years (see, e.g., [29, 27, 15]); we will adapt some of the theoretical results established in these references to our situation. To be precise, we assume that the transmissivity coefficients K_i – which we already supposed to be constant (with respect to space) in each fracture F_i – are known functions of a vector $\mathbf{y} = (y_1, \dots, y_N)$ of N stochastic variables defined in some domain $\mathcal{Y}^N \subseteq \mathbb{R}^N$. We denote by $\mathbf{K} = (K_i)_{1 \leq i \leq I}$ the vector collecting these coefficients.

In order to study how the hydraulic head H depends on these variables via \mathbf{K} , it is convenient to identify H with the vector $\mathbf{H} = (H_i)_{1 \leq i \leq I} \in V^D := \prod_{i=1}^I V_i^D$; we also introduce the vectors

$\mathbf{v} = (v_i)_{1 \leq i \leq I} \in V := \prod_{i=1}^I V_i$ of test functions. Summing-up eqs. (2.1) and using condition (2.3), we see that $\mathbf{H} = \mathbf{H}(\mathbf{y})$ is the solution of the variational problem

$$a(\mathbf{K}(\mathbf{y}); \mathbf{H}(\mathbf{y}), \mathbf{v}) = \langle \Psi, \mathbf{v} \rangle \quad \forall \mathbf{v} \in V, \quad \forall \mathbf{y} \in \mathcal{Y}^N, \quad (3.5)$$

where

$$a(\mathbf{K}; \mathbf{H}, \mathbf{v}) = \sum_{i=1}^I \int_{F_i} K_i \nabla H_i \cdot \nabla v_i, \quad \langle \Psi, \mathbf{v} \rangle = \sum_{i=1}^I \left(\int_{F_i} q_i v_i + \langle G_i^N, v_i|_{\Gamma_{iN}} \rangle \right).$$

For future convenience, we have highlighted the dependence upon \mathbf{K} of the bilinear form a . Note that Ψ does not depend on \mathbf{y} since our boundary and source data are assumed to be deterministic.

We now assume that the transmissivity coefficients are bounded from above and below uniformly in $\mathbf{y} \in \mathcal{Y}^N$, i.e., there exist constants $\kappa_{\min} > 0$ and $\kappa_{\max} > 0$ such that

$$\kappa_{\min} \leq K_i(\mathbf{y}) \leq \kappa_{\max} \quad 1 \leq i \leq I, \quad \forall \mathbf{y} \in \mathcal{Y}^N. \quad (3.6)$$

This implies that the quantity $\|\mathbf{v}\|_{a,\mathbf{y}} := \sqrt{a(\mathbf{K}(\mathbf{y}); \mathbf{v}, \mathbf{v})}$, defined in the larger space $\hat{V} := \prod_{i=1}^I H^1(F_i)$, is uniformly equivalent to the norm $\|\mathbf{v}\|_V := \left(\sum_{i=1}^I \|\nabla v_i\|_{L^2(F_i)}^2 \right)^{1/2}$ in V , precisely

$$\sqrt{\kappa_{\min}} \|\mathbf{v}\|_V \leq \|\mathbf{v}\|_{a,\mathbf{y}} \leq \sqrt{\kappa_{\max}} \|\mathbf{v}\|_V \quad \forall \mathbf{v} \in V, \quad \forall \mathbf{y} \in \mathcal{Y}^N.$$

On the other hand, $\|\mathbf{v}\|_V$ is uniformly equivalent to the norm $\|\mathbf{v}\|_{\hat{V}} := \left(\sum_{i=1}^I \|v_i\|_{H^1(F_i)}^2 \right)^{1/2}$ thanks to our assumption $\Gamma_{iD} \neq \emptyset$ for all $1 \leq i \leq I$. Thus, there exists $C_0 > 0$ independent of \mathbf{y} such that

$$\|\mathbf{v}\|_{\hat{V}} \leq C_0 \|\mathbf{v}\|_{a,\mathbf{y}} \quad \forall \mathbf{v} \in V, \quad \forall \mathbf{y} \in \mathcal{Y}^N. \quad (3.7)$$

Next, we split $\mathbf{H}(\mathbf{y})$ as $\mathbf{H}(\mathbf{y}) = \mathbf{H}^0(\mathbf{y}) + \mathcal{R}\mathbf{H}^D$ with $\mathbf{H}^0(\mathbf{y}) \in V$ and $\mathcal{R}\mathbf{H}^D \in V^D$. Substituting in (3.5) and choosing $\mathbf{v} = \mathbf{H}^0(\mathbf{y})$ therein, we obtain

$$a(\mathbf{K}(\mathbf{y}); \mathbf{H}^0(\mathbf{y}), \mathbf{H}^0(\mathbf{y})) = \langle \Psi, \mathbf{H}^0(\mathbf{y}) \rangle - a(\mathbf{K}(\mathbf{y}); \mathcal{R}\mathbf{H}^D, \mathbf{H}^0(\mathbf{y})).$$

Since there exist constants $c_i > 0$ such that $\|\mathcal{R}_i H_i^D\|_{H^1(F_i)} \leq c_i \|H_i^D\|_{H^{\frac{1}{2}}(\Gamma_{iD})}$ for all $1 \leq i \leq I$, we easily derive the existence of a constant $C_1 > 0$ independent of \mathbf{y} such that

$$\|\mathbf{H}(\mathbf{y})\|_{\hat{V}} \leq C_1 \left(\|\mathbf{q}\|_{L^2} + \|\mathbf{H}^D\|_{H^{\frac{1}{2}}} + \|\mathbf{G}^N\|_{H^{-\frac{1}{2}}} \right), \quad \forall \mathbf{y} \in \mathcal{Y}^N, \quad (3.8)$$

where

$$\|\mathbf{q}\|_{L^2}^2 := \sum_{i=1}^I \|q_i\|_{L^2(F_i)}^2, \quad \|\mathbf{H}^D\|_{H^{\frac{1}{2}}}^2 := \sum_{i=1}^I \|H_i^D\|_{H^{\frac{1}{2}}(\Gamma_{iD})}^2, \quad \|\mathbf{G}^N\|_{H^{-\frac{1}{2}}}^2 := \sum_{i=1}^I \|G_i^N\|_{H^{-\frac{1}{2}}(\Gamma_{iN})}^2.$$

We now assume that \mathbf{K} is an analytic function of \mathbf{y} , and we obtain bounds on the partial derivatives of \mathbf{H} with respect to the components of \mathbf{y} , that imply the analyticity of \mathbf{H} . To this end, we first observe that the quantity $\|\mathbf{H}(\mathbf{y})\|_{a,\mathbf{y}}$ is bounded independently of \mathbf{y} , since it trivially satisfies

$$\|\mathbf{H}(\mathbf{y})\|_{a,\mathbf{y}} \leq \sqrt{\kappa_{\max}} \|\mathbf{H}(\mathbf{y})\|_{\hat{V}} \quad (3.9)$$

and then one uses (3.8). Furthermore, we will use the following Cauchy-Schwarz inequality: if $\mathbf{M}(\mathbf{y}) = (M_i(\mathbf{y}))_{1 \leq i \leq I}$ is any vector depending on \mathbf{y} , then

$$|a(\mathbf{M}(\mathbf{y}); \mathbf{u}, \mathbf{v})| \leq \left\| \frac{\mathbf{M}(\mathbf{y})}{\mathbf{K}(\mathbf{y})} \right\|_{\ell^\infty} \|\mathbf{u}\|_{a,\mathbf{y}} \|\mathbf{v}\|_{a,\mathbf{y}} \quad \forall \mathbf{u}, \mathbf{v} \in \hat{V}, \quad \forall \mathbf{y} \in \mathcal{Y}^N, \quad (3.10)$$

where $\frac{\mathbf{M}(\mathbf{y})}{\mathbf{K}(\mathbf{y})}$ denotes the vector $\left(\frac{M_i(\mathbf{y})}{K_i(\mathbf{y})} \right)_{1 \leq i \leq I}$. The precise assumption on \mathbf{K} is as follows:

$\mathbf{K}(\mathbf{y})$ is differentiable with respect to \mathbf{y} infinitely many times, and there exists a vector $\mathbf{r} \in \mathbb{R}_+^N$ such that

$$\left| \frac{D^\alpha K_i(\mathbf{y})}{K_i(\mathbf{y})} \right| \leq \mathbf{r}^\alpha, \quad 1 \leq i \leq I, \quad \forall \alpha \in \mathbb{N}^N, \quad \forall \mathbf{y} \in \mathcal{Y}^N, \quad (3.11)$$

where $D^\alpha K_i(\mathbf{y}) = \frac{\partial^{|\alpha|} K_i(\mathbf{y})}{\partial y_1^{\alpha_1} \dots \partial y_N^{\alpha_N}}$ with $|\alpha| = \alpha_1 + \dots + \alpha_N$ and $\mathbf{r}^\alpha = r_1^{\alpha_1} \dots r_N^{\alpha_N}$. We will write this assumption as

$$\left\| \frac{D^\alpha \mathbf{K}(\mathbf{y})}{\mathbf{K}(\mathbf{y})} \right\|_{\ell^\infty} \leq \mathbf{r}^\alpha, \quad \forall \alpha \in \mathbb{N}^N, \quad \forall \mathbf{y} \in \mathcal{Y}^N. \quad (3.12)$$

Then, the following result holds (see [27]).

Property 3.1. *Under the previous assumptions on the coefficient vector \mathbf{K} , one has*

$$\|D^\alpha \mathbf{H}(\mathbf{y})\|_{a,\mathbf{y}} \leq d_{|\alpha|} \mathbf{r}^\alpha \|\mathbf{H}(\mathbf{y})\|_{a,\mathbf{y}}, \quad \forall \alpha \neq \mathbf{0}, \quad \forall \mathbf{y} \in \mathcal{Y}^N, \quad (3.13)$$

where the sequence $\{d_m\}_{m \geq 0}$ is defined as

$$d_0 = 1, \quad d_m = \sum_{\ell=0}^{m-1} \binom{m}{\ell} d_\ell.$$

Proof. At first, we observe that $D^\alpha \mathbf{H}(\mathbf{y})$ belongs to V , since the Dirichlet data are assumed to be independent of \mathbf{y} .

Let us begin by proving the inequality for $|\alpha| = 1$. For $1 \leq j \leq N$, we obtain from (3.5), recalling that the right-hand side is independent of \mathbf{y} ,

$$\frac{\partial}{\partial y_j} a(\mathbf{K}(\mathbf{y}); \mathbf{H}(\mathbf{y}), \mathbf{v}) = 0,$$

i.e.,

$$a(\mathbf{K}(\mathbf{y}); \frac{\partial \mathbf{H}}{\partial y_j}(\mathbf{y}), \mathbf{v}) = -a\left(\frac{\partial \mathbf{K}}{\partial y_j}(\mathbf{y}); \mathbf{H}(\mathbf{y}), \mathbf{v}\right) \quad \forall \mathbf{v} \in V.$$

Choosing $\mathbf{v} = \frac{\partial \mathbf{H}}{\partial y_j}(\mathbf{y})$ and using (3.10) with the assumption (3.12) yields

$$\left\| \frac{\partial \mathbf{H}}{\partial y_j}(\mathbf{y}) \right\|_{a,\mathbf{y}}^2 = -a\left(\frac{\partial \mathbf{K}}{\partial y_j}(\mathbf{y}); \mathbf{H}(\mathbf{y}), \frac{\partial \mathbf{H}}{\partial y_j}(\mathbf{y})\right) \leq r_j \|\mathbf{H}(\mathbf{y})\|_{a,\mathbf{y}} \left\| \frac{\partial \mathbf{H}}{\partial y_j}(\mathbf{y}) \right\|_{a,\mathbf{y}},$$

whence the result.

For $|\alpha| > 1$, we use induction upon $|\alpha|$, together with the Faà di Bruno formula for multiple differentiation of a product. We refer to [27], Lemma A.2 for the details. \square

We are ready to state the main result of this section.

Theorem 3.1. *Under the previous assumptions on the coefficient vector \mathbf{K} , the function $\mathbf{H} : \mathcal{Y}^N \rightarrow \hat{V}$ is analytic, i.e., its Taylor expansion centered at any $\mathbf{y}_0 \in \mathcal{Y}^N$ converges to \mathbf{H} in the norm of \hat{V} in a neighborhood of \mathbf{y}_0 .*

Proof. Applying Lemma A.3 in [27], we obtain from (3.13)

$$\|D^\alpha \mathbf{H}(\mathbf{y})\|_{a,\mathbf{y}} \leq |\alpha|! \tilde{\mathbf{r}}^\alpha \|\mathbf{H}(\mathbf{y})\|_{a,\mathbf{y}} ,$$

with $\tilde{\mathbf{r}} = (\log 2)^{-1} \mathbf{r}$. On the other hand, using (3.7) and (3.9), we get

$$\|D^\alpha \mathbf{H}(\mathbf{y})\|_{\hat{V}} \leq C_1 \sqrt{\kappa_{\max}} |\alpha|! \tilde{\mathbf{r}}^\alpha \|\mathbf{H}(\mathbf{y})\|_{\hat{V}} . \quad (3.14)$$

Recalling (3.8), such a growth of the derivatives of $\mathbf{H}(\mathbf{y})$ implies its analyticity; we refer again to [27] for the details. \square

As a final result, we prove that for any discretization of the fracture network, the discrete solution of the optimality system (2.13) is an analytic function of $\mathbf{y} \in \mathcal{Y}^N$. However, the arguments given above cannot be adapted in a straightforward way to this situation; indeed, in the discrete case, the matching conditions (2.2) and (2.3) are not satisfied exactly, preventing us from characterizing the discrete solution via a variational problem similar to (3.5). We rather exploit the property that the matrix

$$\mathcal{M} = \begin{pmatrix} G^h & 0 & A^T \\ 0 & G^u & -\mathcal{B}^T \\ A & -\mathcal{B} & 0 \end{pmatrix}$$

of system (2.13) is nonsingular. Setting for convenience $\mathbf{s} = (h, u, -p)^T$ and $\boldsymbol{\psi} = (0, 0, q)^T$, which are vectors in $\mathbb{R}^{N^{TOT}}$ where $N^{TOT} = 2N^F + N^T$, we write (2.13) as

$$\mathcal{M}(\mathbf{y}) \mathbf{s}(\mathbf{y}) = \boldsymbol{\psi} , \quad (3.15)$$

where we put in evidence the dependence upon \mathbf{y} . Note that the matrices G^h , G^u and \mathcal{B} forming the block-entries of \mathcal{M} do not depend on \mathbf{y} , only A does. Thanks to our assumptions on $\mathbf{K} = \mathbf{K}(\mathbf{y})$, the mapping $\mathbf{y} \mapsto A(\mathbf{y})$ is continuous and bounded from \mathcal{Y}^N to $\mathbb{R}^{N^F \times N^F}$, in particular there exists a constant $D_0 > 0$ such that $\|A(\mathbf{y})\| \leq D_0$ for all $\mathbf{y} \in \mathcal{Y}^N$, where the norm is the one induced by the Euclidean norm in \mathbb{R}^{N^F} . Thus, a similar property holds for $\mathcal{M}(\mathbf{y})$.

Since $\mathcal{M}(\mathbf{y})$ is invertible for any \mathbf{y} ([2]), the matrix $\mathcal{M}^{-1}(\mathbf{y})$ is defined and continuous on \mathcal{Y}^N . From now on, we assume that \mathcal{Y}^N is a compact set. This implies the existence of a constant $D_1 > 0$ independent of \mathbf{y} such that $\|\mathcal{M}^{-1}(\mathbf{y})\| \leq D_1$ for all $\mathbf{y} \in \mathcal{Y}^N$, where the norm is induced by the Euclidean norm in $\mathbb{R}^{N^{TOT}}$. Consequently, we obtain from (3.15)

$$\|\mathbf{s}(\mathbf{y})\| \leq D_1 \|\boldsymbol{\psi}\| , \quad \forall \mathbf{y} \in \mathcal{Y}^N . \quad (3.16)$$

The following result is the counterpart of Property 3.1.

Property 3.2. *Under the previous assumptions on the coefficient vector \mathbf{K} and on \mathcal{Y}^N , one has*

$$\|D^\alpha \mathbf{s}(\mathbf{y})\| \leq D_0 D_1 d_{|\alpha|} \mathbf{r}^\alpha \|\mathbf{s}(\mathbf{y})\| , \quad \forall \alpha \neq \mathbf{0}, \quad \forall \mathbf{y} \in \mathcal{Y}^N .$$

Proof. We check the inequality for $|\alpha| = 1$ only, then one may proceed as in [27]. Differentiating (3.15), we get for $1 \leq j \leq N$

$$\mathcal{M}(\mathbf{y}) \frac{\partial \mathbf{s}}{\partial y_j}(\mathbf{y}) = -\frac{\partial \mathcal{M}}{\partial y_j}(\mathbf{y}) \mathbf{s}(\mathbf{y}) ,$$

which implies

$$\left\| \frac{\partial \mathbf{s}}{\partial y_j}(\mathbf{y}) \right\| \leq D_1 \left\| \frac{\partial \mathcal{M}}{\partial y_j}(\mathbf{y}) \right\| \|\mathbf{s}(\mathbf{y})\| .$$

It is easily seen that

$$\left\| \frac{\partial \mathcal{M}}{\partial y_j}(\mathbf{y}) \right\| \leq \left\| \frac{\partial A}{\partial y_j}(\mathbf{y}) \right\| \leq \left\| \frac{\frac{\partial \mathbf{K}}{\partial y_j}}{\mathbf{K}} \right\|_{\ell^\infty} \|A(\mathbf{y})\| \leq r_j D_0 , \quad \forall \mathbf{y} \in \mathcal{Y}^N ,$$

whence the desired inequality. \square

Using this property, one obtains the following result.

Theorem 3.2. *Under the previous assumptions on the coefficient vector \mathbf{K} and on \mathcal{Y}^N , the mapping $\mathbf{s} : \mathcal{Y}^N \rightarrow \mathbb{R}^{N^{TOT}}$ is analytic.* \square

4. Stochastic collocation and DFNs

In the sequel, we assume that the transmissivity coefficients are random variables that obey certain prescribed laws. For a given incoming flux, we are interested in evaluating the probability that the outgoing flux assumes a certain directionality. To this end, we will monitor mean value and variance of the flux across specific fracture edges.

4.1. The geometry

We consider representative DFNs, composed by a set of I rectangular fractures, sharing the following common structure.

A fracture labeled F_1 lies on the x_1 - x_2 plane. We set $F_1 = [0, 1] \times [0, 1]$. All other fractures are orthogonal to the x_1 - x_2 plane, and in particular fracture F_2 is parallel to the east edge of F_1 , whereas fracture F_3 is parallel to the north edge of F_1 . Additional fractures F_i , $i = 4, \dots, I$, connect the network. Fig. 1 shows an example of network: on the left, the 3D view is depicted, and traces are highlighted; on the right, the projection of the DFN on the x_1 - x_2 plane is drawn.

Numerical experiments will be performed using the two geometries shown in Fig. 2. On the left, 7 fractures are considered; all edges of fractures F_4, \dots, F_7 are chosen of length 1.5. On the right, we have 12 fractures, with edge lengths equal to 1.2 for fractures F_4 to F_{12} . In both cases, the figure shows the numbering of the additional fractures F_i , for $i = 4, \dots, I$. We point out that we deliberately consider rather simple networks, in order to ease the understanding of the overall stochastic behavior; nonetheless, our approach may be applied to realistic networks as well.

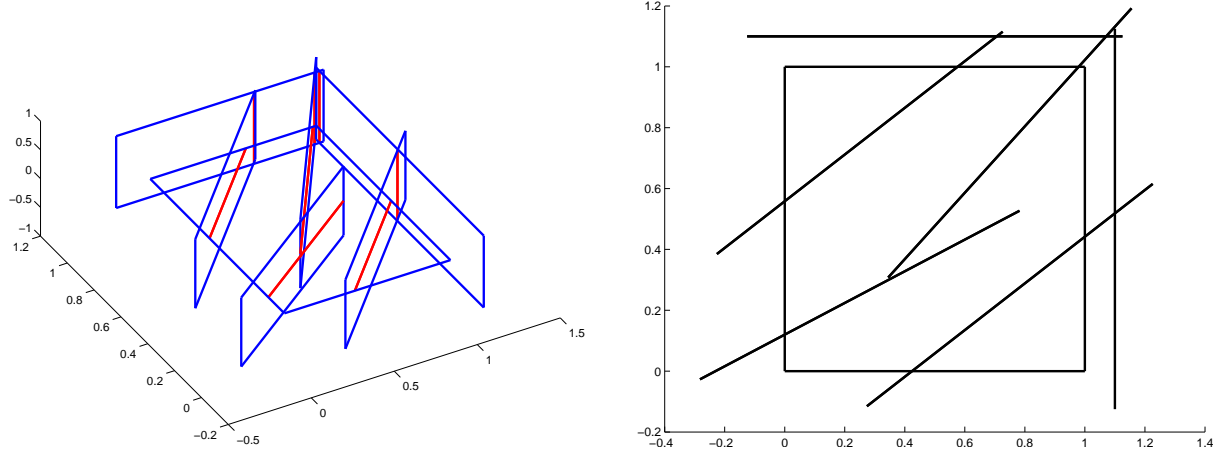


Figure 1: Example of simple network. Left: 3D view (traces in red); right: projection on the x_1-x_2 plane

4.2. The problem

With reference to eq. (2.6), we consider a problem with a null source term q ; a constant incoming flux is imposed on the west edge $E_{1,w}$ of the horizontal fracture F_1 , precisely we set $(\partial H_1 / \partial \hat{\nu}_1) = 10$ on $E_{1,w}$. The Dirichlet boundary is composed of two fracture edges: the east edge $E_{2,e}$ of fracture F_2 and the west edge $E_{3,w}$ of fracture F_3 (their projections on the x_1-x_2 plane are highlighted by circles in Fig. 2), where the constant Dirichlet values $H_2 = 100$ and $H_3 = 200$, respectively, are enforced. Homogeneous Neumann conditions are imposed on all the remaining parts of the boundary. Within this simple configuration, the fluid entering the network through the non-homogeneous Neumann boundary on F_1 , flows through the network and affects, among others, fractures F_2 and F_3 . Variations in the hydraulic properties of the DFN yield variations of flux directionality. Hence, we are interested in measuring how the flux distributes between F_2 and F_3 .

For $i = 1, 2, 3$, let us denote by $\Phi^{(i)}$ the total flux entering fracture F_i through its traces. Note that, since all other edges of F_1 are assumed to be insulated (i.e., homogeneous Neumann conditions are imposed therein), $\Phi^{(1)}$ equals the opposite of the total flux entering F_1 through

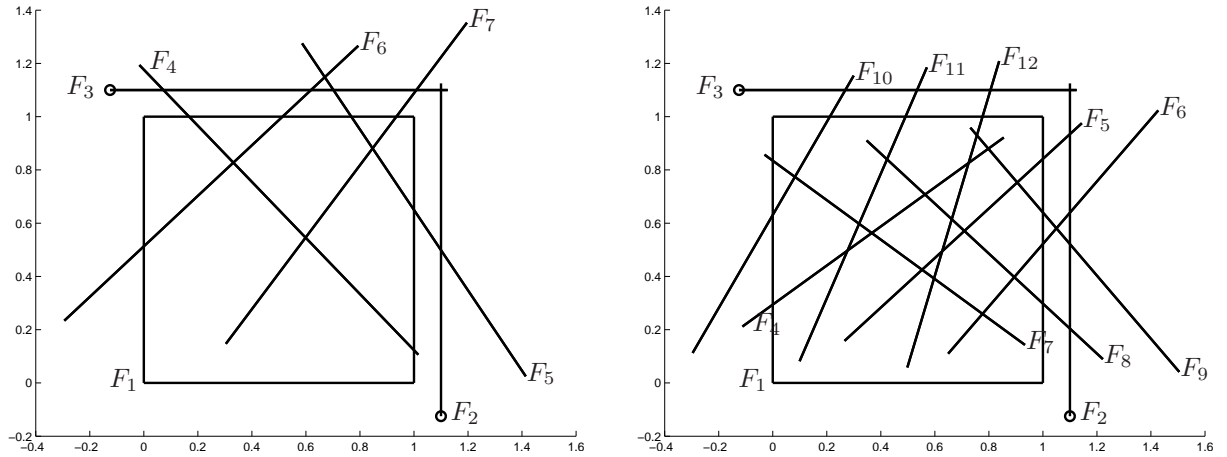


Figure 2: Projection on the x_1-x_2 plane of the DFNs used in our test cases. Left: tests T1-T2; right: tests T3-T5

$E_{1,w}$, i.e.,

$$\Phi^{(1)} = - \int_{E_{1,w}} \frac{\partial H_1}{\partial \hat{\nu}_1} = -10$$

(recall that $E_{1,w}$ has unit length). For similar reasons, $\Phi^{(i)}$, $i = 2, 3$, equals the opposite of the total flux leaving F_i through its Dirichlet edge, i.e.,

$$\Phi^{(2)} = - \int_{E_{2,e}} \frac{\partial H_2}{\partial \hat{\nu}_2}, \quad \Phi^{(3)} = - \int_{E_{3,w}} \frac{\partial H_3}{\partial \hat{\nu}_3}. \quad (4.1)$$

Furthermore, due to flux conservation within the network, since non-homogeneous Neumann conditions or Dirichlet conditions are imposed only on the boundaries of F_1 , F_2 , F_3 , the sum $\Phi^{(1)} + \Phi^{(2)} + \Phi^{(3)}$ vanishes.

The discrete counterparts of the total fluxes $\Phi^{(i)}$, $i = 1, 2, 3$, will be denoted by $\phi^{(i)}$ and will be monitored in our numerical experiments. For accuracy reasons, they are computed by the formula $\phi^{(i)} = \sum_{S_m \in \mathcal{S}_i} \int_{S_m} u_m^i$, where u is defined by (2.13).

Remark 4.1. *The finite element discretization used herein is based on Extended Finite Elements as shown in [4]. The mesh parameter δ , used to characterize mesh element sizes, corresponds to the maximum element area of the underlying mesh and is the same for all fractures except for F_1 , F_2 , F_3 . Indeed, since in the networks considered herein fracture F_1 typically hosts several traces, we use on F_1 a maximum element size which is 0.25 times the maximum element size used on the other fractures. Furthermore, since discretizations on traces are induced by discretizations on fractures, finer meshes are built on fractures F_2 and F_3 as well for increasing the accuracy in the computation of $\phi^{(2)}$ and $\phi^{(3)}$.*

Since we are interested in studying the behavior of the stochastic approach described herein, in order to prevent the numerical results from being affected by the choice of stopping criterion and related parameters required by gradient-like methods, we performed each simulation by solving the KKT system (2.13) by a direct method.

The accuracy of the stochastic collocation method in approximating the quantities of interest $\Phi^{(i)}$, $i = 2, 3$, depends on their smoothness with respect to the stochastic variable \mathbf{y} . The following analyticity result is a consequence of the smoothness of the function \mathbf{H} , established in Theorem 3.1. For the sake of simplicity, we only deal with the quantity $\Phi^{(2)}$.

Property 4.1. *Let the transmissivity vector \mathbf{K} satisfy assumptions (3.6) and (3.11), and suppose that the east edge $E_{2,e}$ of fracture F_2 is not a trace of the network. Then, the total flux $\Phi^{(2)} = \Phi^{(2)}(\mathbf{y})$ defined in (4.1) is an analytic function in \mathcal{Y}^N .*

Proof. Consider a rectangular subfracture $F'_2 \subset F_2$ having the right-hand vertical edge coinciding with $E_{2,e}$ and the opposite edge at a positive distance from the traces on F_2 . Since $q = 0$ everywhere, the head H_2 is harmonic in F'_2 ; furthermore, it fulfills such boundary conditions (constant Dirichlet on $E_{2,e}$, homogeneous Neumann on the upper and lower horizontal edges of F_2) that guarantee the H^2 -regularity of H_2 in F'_2 , thanks to the regularity theory for elliptic problems in polygonal domains (see, e.g., [30]). Precisely, taking into account (3.8), there exists a constant $C_2 > 0$ such that

$$\|H_2(\mathbf{y})\|_{H^2(F'_2)} \leq C_2 \quad \forall \mathbf{y} \in \mathcal{Y}^N.$$

Level	Gauss-Patterson grid						Kronrod-Patterson-Normal grid					
	$N = 1$		$N = 2$		$N = 4$		$N = 1$		$N = 2$		$N = 4$	
0	1	1	1	1	1	1	1	1	1	1	1	1
1	2	3	4	5	8	9	2	3	4	5	8	9
2	4	7	12	17	40	49	6	9	16	21	48	57
3	8	15	32	49	160	209	10	19	44	65	216	273
4	16	31	80	129	560	769	16	35	108	173	824	1097
5	32	63	192	321	1792	2561	-	-	-	-	-	-
6	64	127	448	769	5376	7937	-	-	-	-	-	-

Table 1: Number of nodes used in the sparse grids

Any derivative $D^\alpha H_2(\mathbf{y})$ with respect to the stochastic variables is harmonic in F'_2 as well, and fulfills homogeneous boundary conditions near $E_{2,e}$ of the same type as those satisfied by H_2 ; hence, again we obtain H^2 -regularity in F'_2 , i.e., by (3.14) and (3.8)

$$\|D^\alpha H_2(\mathbf{y})\|_{H^2(F'_2)} \leq C_3 |\alpha|! \tilde{\mathbf{r}}^\alpha \quad \forall \alpha \neq \mathbf{0}, \quad \forall \mathbf{y} \in \mathcal{Y}^N.$$

This implies that the mapping $\mathbf{y} \mapsto H_2(\mathbf{y})$ is analytic from \mathcal{Y}^N to $H^2(F'_2)$. Consequently, its restriction $H_2(\mathbf{y})|_{E_{2,e}}$ is analytic from \mathcal{Y}^N to $H^{1/2}(E_{2,e}) \subset L^2(E_{2,e})$, whence the result. \square

4.3. Generation of sparse grids

We will consider two probability densities for the random transmissivity coefficients: log-uniform and log-normal, meaning that the logarithms of the random coefficients with respect to a chosen basis will be either uniformly distributed or distributed according to a Gaussian. The corresponding collocation/quadrature grids are chosen as follows.

For the uniform distribution, we use the Gauss-Patterson grids [23], which are nested grids: given a rule with m nodes, $m + 1$ nodes are added in such a way that the order of polynomial accuracy of the new formula is maximal, i.e., at least $3m + 1$. The sequence is started at level 0 with one node (the mid-point of the interval); at level 1, two nodes are added in such a way that the three nodes obtained are the nodes of the 3-point Gauss-Legendre rule; at next levels, the sequence is produced following the Patterson rule. The maximum level used herein is 6, corresponding to a total of 127 nodes in the 1D case. All weights are in this case positive, see also [31].

For the normal distribution, we use the Kronrod-Patterson-Normal (KPN) nodes [25], in order to take advantage from nested formulas. For KPN nodes the maximum attainable level is 4, corresponding in the 1D case to 35 nodes.

Multi-dimensional sparse quadrature formulas are then built according to Smolyak's recipe as shown in Sect. 3. Clearly, also in this case grids are nested, and in Table 1 we report, for various values of dimension N , both the number of nodes added at each level (left columns) and the total number of nodes (right columns). In our computations, we use sparse grids generated by the `spinterp` library [32, 33] for the uniform distribution and the `sparse grid toolkit` [34, 29] for the normal distribution.

We are now ready to present the results of a first set of test cases, designed within the framework described so far. Next section will provide additional test cases.

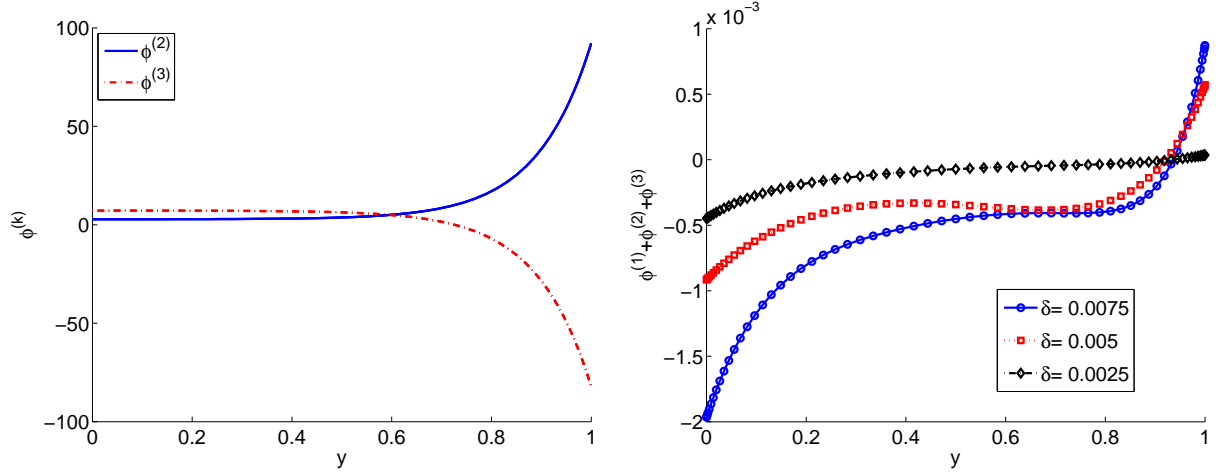


Figure 3: Test T1. Left: computed values of $\phi^{(2)}$ and $\phi^{(3)}$ versus y ; right: computed values of $\phi^{(1)} + \phi^{(2)} + \phi^{(3)}$ versus y .

4.4. Test case T1

As a preliminary investigation, we consider a DFN with $I = 7$ fractures, whose projections on the x_1 - x_2 plane are shown in Fig. 2, left. The stochastic transmissivities are not considered independent processes, as the same transmissivity K is set on all fractures, and it is assumed to be a function of a unique stochastic parameter. More in details, we consider a random variable Y with uniform distribution in $[0, 1]$ and we assume

$$K(\omega) = 10^{L_{\min} + (L_{\max} - L_{\min})Y(\omega)}, \quad Y \sim \mathcal{U}([0, 1])$$

with $L_{\min} = -4$ and $L_{\max} = 0$.

In Fig. 3, left, we plot, versus the image y of the random variable Y , the values $\phi^{(2)}$ and $\phi^{(3)}$ computed on the sparse grid obtained at level 6 and on the finest finite element mesh used. In Fig. 3, right, we report the values of $\phi^{(1)} + \phi^{(2)} + \phi^{(3)}$ computed for all the finite element mesh sizes considered for this test problem, and on the sparse grid of level 6. It can be noticed that flux balance is well reproduced, and that decreasing the finite element mesh size does improve the numerical flux balance. Since $\phi^{(1)}$ is deterministic, i.e., independent of \mathbf{y} , the sum $\phi^{(2)} + \phi^{(3)}$ is (nearly) constant, as documented by the left plots.

The errors on $\mathbb{E}(\phi^{(k)})$ and $\sigma^2(\phi^{(k)})$, $k = 2, 3$, are plotted in Fig. 4 versus the cardinality of the sparse grid, for different choices of the space mesh parameter δ . Errors are computed w.r.t. a reference solution obtained using the finest sparse grid (i.e., the one corresponding to level 6). It is clearly noted that errors decrease quite rapidly up to level 3 with an exponential decay, reaching errors of order $\sim 10^{-11}$ – 10^{-12} ; this behavior is coherent with the analyticity of $\Phi^{(k)}$ in the \mathbf{y} variable, established in Property 4.1. Afterwards, the convergence breaks down and essentially no progress is made towards reaching double precision roundoff error. This is clearly due to numerical effects related to the ill-conditioning of the KKT system, which prevents from further improving the accuracy. It is worth noting that for the finite element meshes here considered, results are nearly independent of the mesh size.

In the same figure, we also compare the errors with those obtained by the Monte Carlo method. Namely, we consider M independent and identically distributed realizations $K(\omega_s)$,

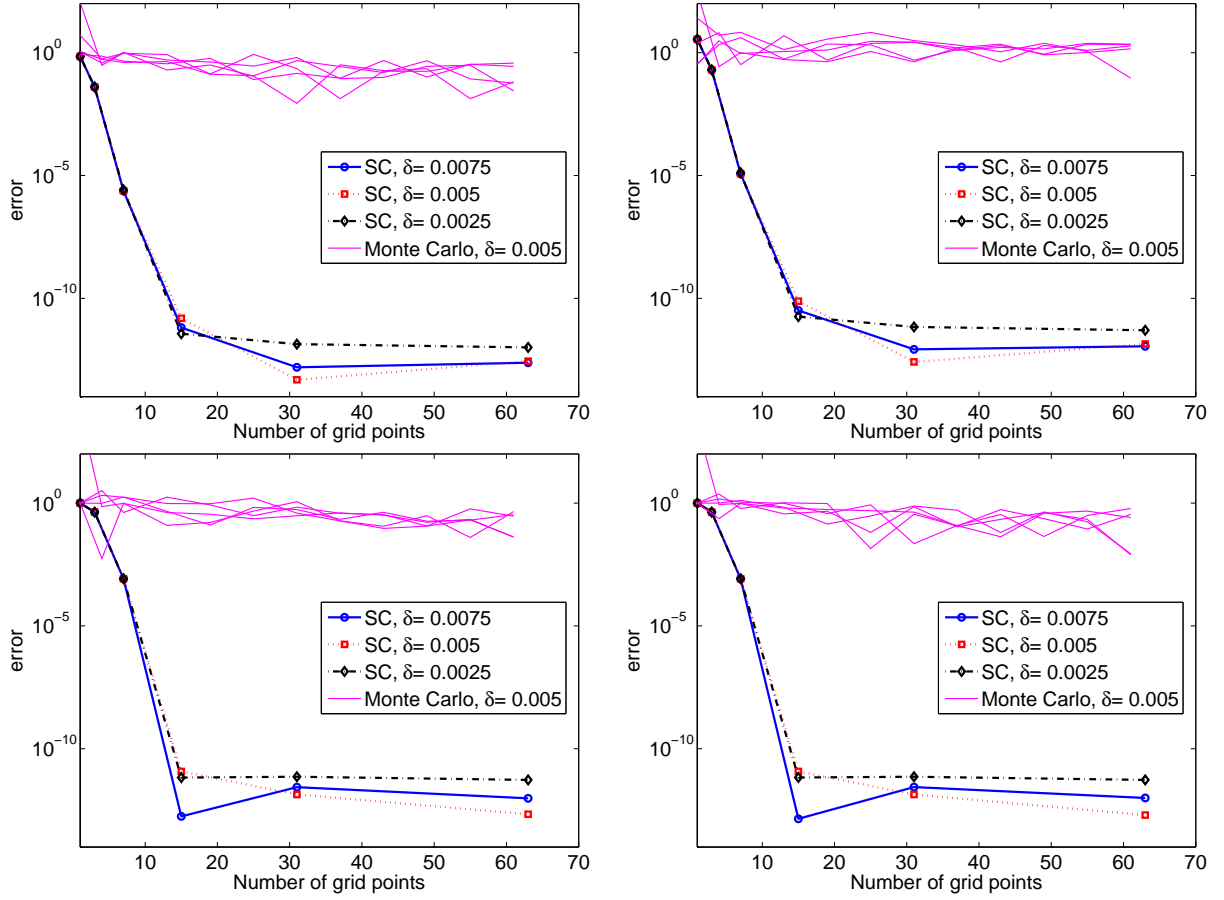


Figure 4: Test T1, convergence curves for different values of the space discretization parameter δ . Top: mean value, bottom: variance. Left: $\phi^{(2)}$, right: $\phi^{(3)}$.

$s = 1, \dots, M$, of the transmissivity, and then we compute the sample average and variance:

$$\bar{\mathbb{E}}_M(\phi^{(k)}) = \frac{\sum_{s=1}^M \phi^{(k)}(K(\omega_s))}{M}, \quad \bar{\sigma}_M^2(\phi^{(k)}) = \frac{\sum_{s=1}^M (\phi^{(k)}(K(\omega_s)))^2}{M} - \bar{\mathbb{E}}_M^2(\phi^{(k)}).$$

Errors are then computed w.r.t. the reference solution obtained by the stochastic collocation approach. Plots reported in Fig. 4, which refer to 5 different realizations, are obtained with the finite element grid with mesh parameter $\delta = 0.005$; for them, values on the x -axis correspond to M . The present test case is obviously particularly favorable for the stochastic collocation method, which is documented in a limpid way by our results.

4.5. Test case T2

In this second test case, again with the geometry shown in Fig. 2, left, we set a fixed value for the transmissivity on fractures F_1 , F_2 and F_3 , whereas we assume that each of the pairs of fractures F_4 – F_5 and F_6 – F_7 has the same transmissivity, given by a stochastic process whose logarithm follows a uniform distribution; precisely, if $Y_\alpha \sim \mathcal{U}([0, 1])$, $\alpha = 1, 2$, are independent variables, we set

$$K_i = 10^{-2}, \quad i = 1, 2, 3, \quad K_4(\omega) = K_5(\omega) = 10^{L(Y_1(\omega))}, \quad K_6(\omega) = K_7(\omega) = 10^{L(Y_2(\omega))},$$

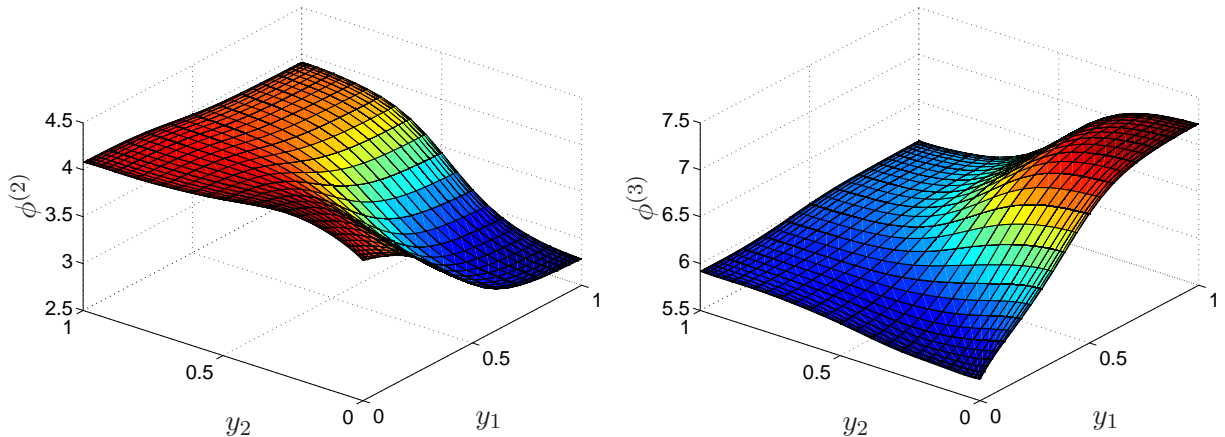


Figure 5: Test case T2: $\phi^{(2)}$ (left) and $\phi^{(3)}$ (right) versus the stochastic parameters y_1 and y_2

where

$$L(Y_\alpha(\omega)) = L_{\min} + (L_{\max} - L_{\min})Y_\alpha(\omega) ,$$

with $L_{\min} = -4$, $L_{\max} = 0$. This apparently artificial assumption, i.e., that a group of fractures shares the same transmissivity, has actually a counterpart in real applications: indeed, in a real network it appears more realistic to have groups of fractures with similar geological properties, hence similar transmissivity, rather than individual fractures with completely independent transmissivities.

A 2-dimensional sparse grid is used for these computations, and again three different space mesh parameters have been used for this test case, namely $\delta = 0.0075$, $\delta = 0.005$ and $\delta = 0.0025$.

In Fig. 5, we plot $\phi^{(2)}$ and $\phi^{(3)}$ for $\delta = 0.0025$ versus the two stochastic parameters y_1 and y_2 , whereas in Fig. 6 we plot the errors on $\mathbb{E}(\phi^{(k)})$ and $\sigma^2(\phi^{(k)})$, $k = 2, 3$. Errors are computed w.r.t. a reference solution obtained on the finest sparse grid (i.e., the one corresponding to level 6). In a comparison with Test case T1, it may be noted that the influence of the spatial grid is only slightly more pronounced, whereas the attained errors are significantly larger. This deterioration of convergence, as the number of stochastic dimensions increases, is well documented in the literature (see, e.g., [20]); nonetheless, the reduction of the errors is still quite fast. Again, the same figure reports the behavior of the Monte Carlo method. The stochastic collocation approach yields smaller errors also in this case, although the gain w.r.t. to Monte Carlo is not as remarkable as in Test T1; indeed, as expected, the behavior of the Monte Carlo method is not affected by the dimensionality of the problem.

5. Towards higher stochastic dimensions

In this last section, we move towards richer networks, in which the distribution of random transmissivities is defined via a Karhunen-Loève expansion determined by the assignment of a certain covariance function.

To be precise, we assume that the transmissivity $K_i(\omega)$ of each fracture F_i with $i \geq 4$ is again constant in space and is determined by the position of the center of mass \mathbf{x}_i of the fracture. Since our vertical fractures are symmetrically placed across the horizontal plane $x_3 = 0$, these centers of mass belong to a region D in the x_1 - x_2 plane, containing fracture F_1 . Thus, we set

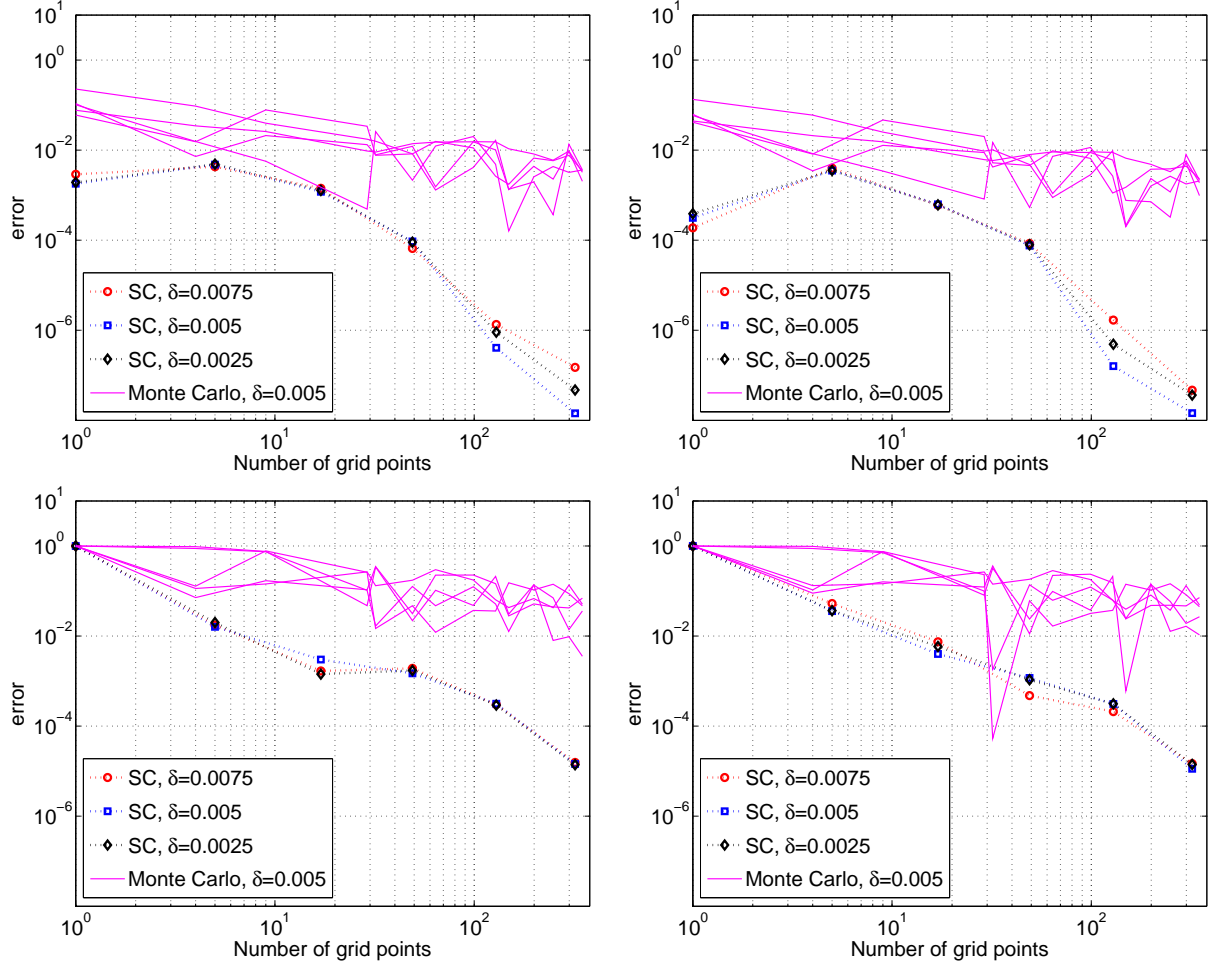


Figure 6: Test case T2, convergence curves on moments versus the number of nodes of the sparse grid. Top: mean value, bottom: variance. Left: $\phi^{(2)}$, right: $\phi^{(3)}$.

$K_i(\omega) = K(\mathbf{x}_i, \omega)$, where

$$K(\mathbf{x}, \omega) = b^{L(\mathbf{x}, \omega)}, \quad \text{with } L : (\mathbf{x}, \omega) \in D \times \Omega \mapsto L(\mathbf{x}, \omega) \in \mathbb{R},$$

being $b > 1$ a fixed constant. We suppose that we know the covariance function $C_L(\mathbf{x}, \mathbf{z})$ of $L = \log_b K$, i.e., the function

$$C_L(\mathbf{x}, \mathbf{z}) = \mathbb{E}[(L(\mathbf{x}, \cdot) - \mathbb{E}[L](\mathbf{x}))(L(\mathbf{z}, \cdot) - \mathbb{E}[L](\mathbf{z}))], \quad \mathbf{x}, \mathbf{z} \in D.$$

Assuming C_L continuous on $D \times D$, let $\varphi_n(\mathbf{x})$, $n \geq 1$, be the orthonormal eigenfunctions, with corresponding positive and non-increasing eigenvalues λ_n , of the compact operator $T\varphi = \int_D C_L(\cdot, \mathbf{z})\varphi(\mathbf{z})d\mathbf{z}$. Then, the Karhunen-Loève decomposition of L is

$$L(\mathbf{x}, \omega) = \mathbb{E}[L](\mathbf{x}) + \sum_{n=1}^{\infty} \sqrt{\lambda_n} \varphi_n(\mathbf{x}) Y_n(\omega), \quad (5.1)$$

where Y_n are mutually uncorrelated random variables satisfying $\mathbb{E}[Y_n] = 0$, $\mathbb{E}[Y_n^2] = 1$. Since the expansion contains infinitely many terms, we apply a truncation of the series after the first

$\gamma = 0.25$	$\gamma = 1.5$
1.680130e-1	1.185118e+0
1.331237e-1	1.160702e-1
1.331237e-1	1.160702e-1
1.054795e-1	1.136799e-2
9.062758e-2	5.028128e-3
9.062758e-2	5.028128e-3
7.180801e-2	4.924540e-4
7.180801e-2	4.924540e-4
5.328330e-2	1.384869e-4
5.328330e-2	1.384869e-4
4.888524e-2	2.133296e-5

Table 2: Largest eigenvalues of the operator T for the covariance given by (5.2)

N terms, for some $N \geq 1$, thus defining a finite expansion $L_N(\mathbf{x}, \omega)$ that replaces $L(\mathbf{x}, \omega)$ in the previous definition of transmissivity. The truncation parameter N hereby represents the stochastic dimension of our problem. Obviously, the faster is the decay of the eigenvalues, the smaller is the value of N needed for a good approximation. This in turn depends on the smoothness of the correlation kernel $C_L(\mathbf{x}, \mathbf{z})$ and the size of the correlation length.

In the sequel, we choose $D = [0, 1.2] \times [0, 1.2]$ and consider a covariance function given by

$$C_L(\mathbf{x}, \mathbf{z}) = e^{-\frac{\|\mathbf{x}-\mathbf{z}\|^2}{\gamma^2}}, \quad \mathbf{x}, \mathbf{z} \in D, \quad (5.2)$$

the parameter γ being a measure of correlation length. Focusing on two values of the correlation length, namely $\gamma = 0.25$ and $\gamma = 1.5$, the largest eigenvalues of T (numerically computed) are listed in Table 2. Note how a larger correlation length induces a faster decay of the eigenvalues.

Hereafter, we present some numerical experiments relative to a DFN with $I = 12$ fractures, whose projections on the x_1 - x_2 plane are shown in Fig. 2, right. The transmissivities of the fractures F_i for $i = 1, 2, 3$ will be invariably set to the value 10^{-2} .

5.1. Test case $T3$

For $i \geq 4$, we consider the transmissivities

$$K_{i,N}(\omega) = 10^{L_{i,N}(Y_1(\omega), \dots, Y_N(\omega))}, \quad L_{i,N}(Y_1(\omega), \dots, Y_N(\omega)) = 10^{-2} + \sum_{n=1}^N \sqrt{\lambda_n} \varphi_n(\mathbf{x}_i) Y_n(\omega), \quad (5.3)$$

where $Y_n(\omega)$ are uniformly distributed independent random variables, such that $\mathbb{E}[Y_n] = 0$ and $\mathbb{E}[Y_n^2] = 1$, hence $Y_n \sim \mathcal{U}([-\sqrt{3}, \sqrt{3}])$; indeed, if $\tilde{Y}_n(\omega)$ is a random variable such that $\tilde{Y}_n \sim \mathcal{U}([0, 1])$ (hence $\mathbb{E}[\tilde{Y}_n] = \frac{1}{2}$ and $\mathbb{E}[\tilde{Y}_n^2] = \frac{1}{12}$), then $Y_n(\omega) = \sqrt{3}(2\tilde{Y}_n(\omega) - 1)$.

In Fig. 7, left, we report the values of $\phi^{(2)}$ and $\phi^{(3)}$ versus \tilde{y}_1 in the case $N = 1$. We used a space grid with maximum element size $\delta = 0.0025$ and the Gauss-Patterson sparse grid corresponding to level 4. Fig. 7, right, shows a plot of $\phi^{(3)}$ versus \tilde{y}_1 and \tilde{y}_2 for the case $N = 2$ and $\gamma = 0.25$.

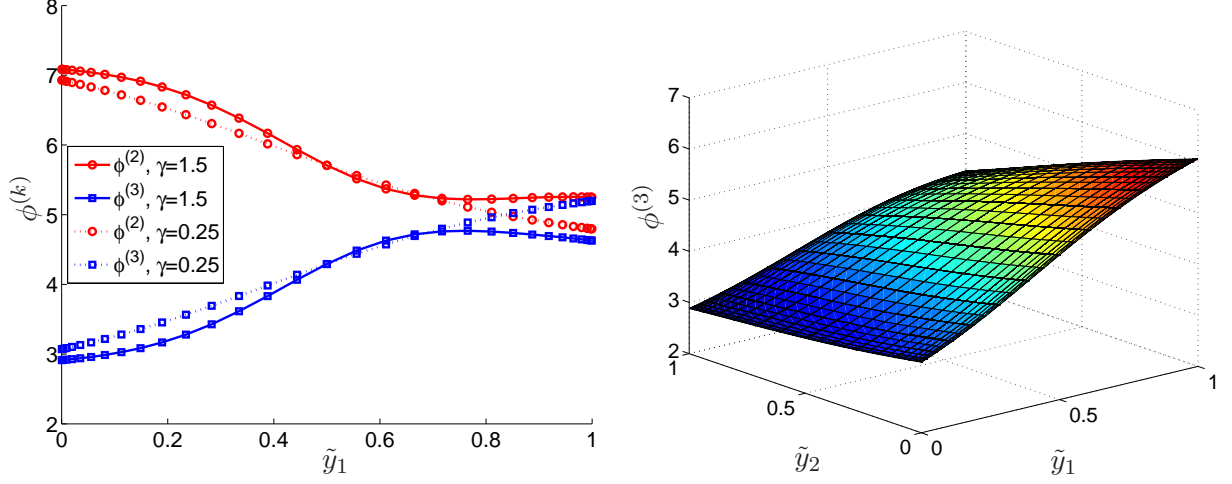


Figure 7: Test case T3: computed values of $\phi^{(2)}$ and $\phi^{(3)}$ versus \tilde{y}_1 , $N = 1$ (left) and of $\phi^{(3)}$ versus \tilde{y}_1 and \tilde{y}_2 , $N = 2$, $\gamma = 0.25$ (right).

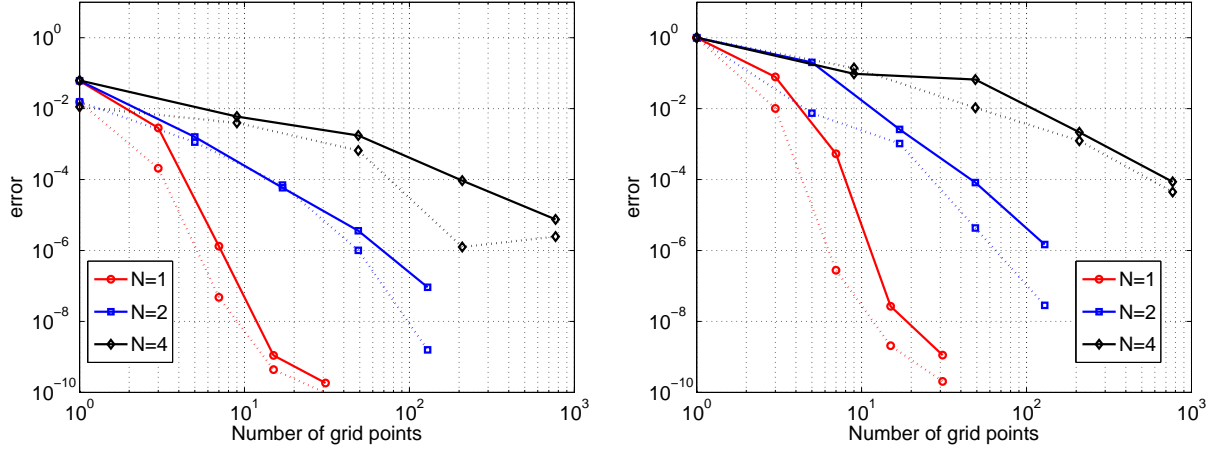


Figure 8: Test case T3: convergence curves on moments of $\phi^{(3)}$ w.r.t. number of nodes in the sparse grid. Left: mean value, right: variance; $\gamma = 1.5$ (continuous line) and $\gamma = 0.25$ (dotted line).

Since the behaviors of $\phi^{(2)}$ and $\phi^{(3)}$ are similar, from now on we monitor just one of them, precisely the latter. The convergence curves of the mean value and the variance are reported in Fig. 8. It may be noted that dotted lines (corresponding to the smaller value of γ) decay slightly faster than solid lines; this behavior is coherent with the plots in Fig. 7, left, where the functions $\phi^{(k)}$ for $\gamma = 0.25$ are slightly smoother than those for $\gamma = 1.5$ (see [20] for a rigorous explanation of such a behavior in a slightly different context).

For $N = 2$ (blue plots), a comparison with the results of Test case 2 (Fig. 6, right) is meaningful, and indicates that the convergence rates of the errors are similar in the two cases.

At last, Fig. 8 clearly demonstrates the already mentioned curse of dimensionality: increasing the stochastic dimensionality results in a significant reduction of the overall accuracy for a fixed cost of the simulation (proportional to the number of points in the sparse grid). Test case 5 will indicate how to cure this drawback.

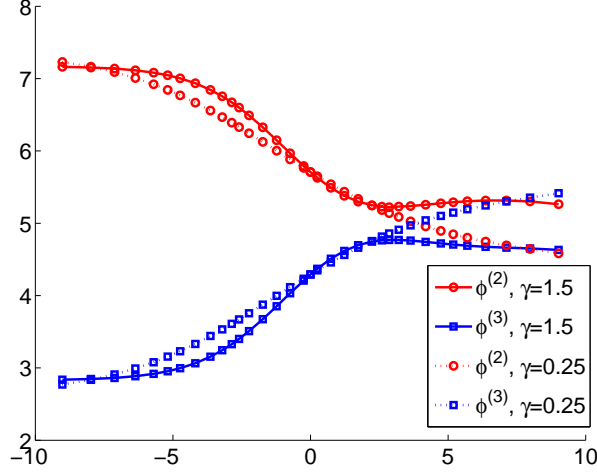


Figure 9: Test case T4: computed values of $\phi^{(2)}$ and $\phi^{(3)}$ versus y_1 , $N = 1$.

5.2. Test case T4

This test is similar to Test case T3 except for the distribution of the random variables Y_n which are here assumed to have a normal distribution; precisely, we set

$$K_{i,N}(\omega) = 2^{L_{i,N}(Y_1(\omega), \dots, Y_N(\omega))}, \quad L_{i,N}(Y_1(\omega), \dots, Y_N(\omega)) = L_0 + \sum_{n=1}^N \sqrt{\lambda_n} \varphi_n(\mathbf{x}_i) Y_n(\omega) \quad (5.4)$$

with $Y_n \sim \mathcal{N}(0, 1)$. Here, $b = 2$ rather than $b = 10$ is used in order to guarantee a range of variability of $K_{i,N}$ comparable to that of the uniform distribution (keeping into account the largest interval containing the nodes of the finest Kronrod-Patterson-Normal grid in 1D). We set $L_0 = -2\log_2(10)$ so that when $y_n = Y_n(\omega) = 0$ for $n = 1, \dots, N$ we have $K_{i,N} = 10^{-2}$ as in Test case T2.

In Fig. 9 we report the values of $\phi^{(2)}$ and $\phi^{(3)}$ versus y_1 in the case $N = 1$. We used a space grid with maximum element size $\delta = 0.0025$ and the Kronrod-Patterson-Normal sparse grid with maximum level 4. The convergence curves of the mean value and the variance of $\phi^{(3)}$ are reported in Fig. 10. Results appear to be qualitatively similar to those of Test case T3.

5.3. Test case T5: anisotropic grids

As it is clear from the previous examples, when the number of stochastic variables increases, the number of simulations to be performed rapidly grows even with sparse grids. Furthermore, it is known (see e.g. [26] and the references therein) that the convergence rate of sparse collocation deteriorates in problems exhibiting an intrinsically anisotropic nature. This is the case, e.g., of (truncated) Karhunen-Loève decompositions of stochastic processes with large correlation lengths, in which the fast decay of the eigenvalues λ_n reduces the influence of the corresponding stochastic variables y_n . Following [26], and keeping the same framework of Test case T4, we propose here a few results obtained by using anisotropic grids. We consider the case $\gamma = 1.5$, for which the anisotropic structure of the random process is more evident, and we investigate the stochastic dimensions $N = 6, 10, 20$. The choice of the vector of weight parameters β in (3.4) has been heuristically guided by the clustered distribution of values $\sqrt{\lambda_n} \varphi(\mathbf{x}_i)$ appearing in (5.4), averaged over the fractures. Namely, we allow for the same kind of refinement along

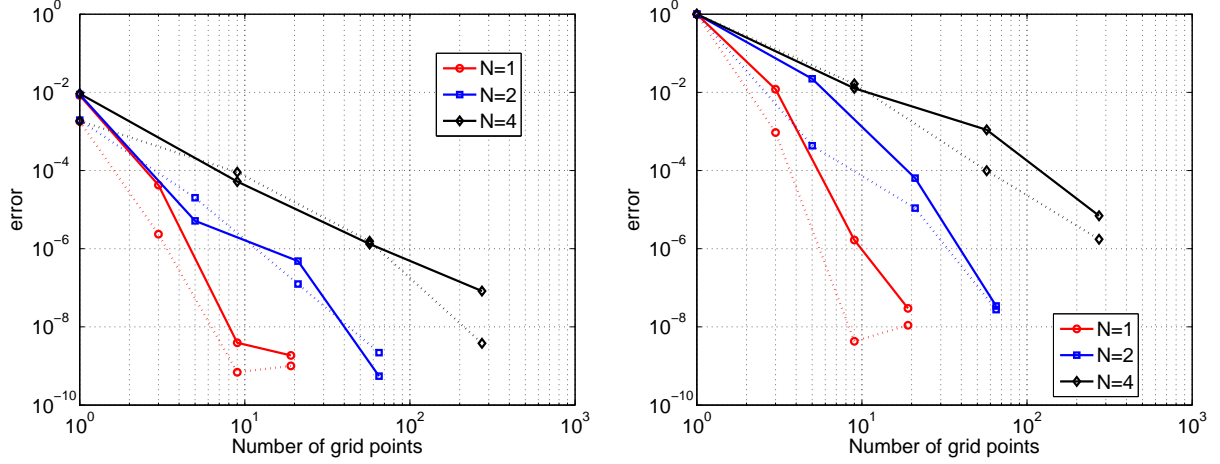


Figure 10: Test case T4: convergence curves on moments of $\phi^{(3)}$ w.r.t. number of nodes in the sparse grid. Left: mean value, right: variance; $\gamma = 1.5$ (continuous line) and $\gamma = 0.25$ (dotted line).

the first three stochastic dimensions, and then we gradually reduce the refinement. The values of β_k used for the k -th stochastic variable are listed in Table 3, along with the corresponding maximum level of refinement attained for $w = 3$. The reference solution has been computed with $w = 4$ and with smaller values for parameters β_k , for $k \geq 4$.

Fig. 11 quantifies for a fixed stochastic dimension the gain in efficiency produced by replacing isotropic sparse grids by anisotropic ones. Fig. 12 provides a clear-cut demonstration that, at least for the higher stochastic dimensions here considered, the curse of dimensionality may be successfully contrasted by a clever selection of anisotropic grids.

6. Conclusions

We have considered flows in fractured media, in particular we have focussed on the flow computation in fractures. To this aim, the DFN model for fractured media has been used. Due to the computational complexity of this approach, the flow computations are usually performed in a purely deterministic way. To overcome such a limitation, we have applied modern Uncertainty Quantification techniques to estimate the uncertainty in the model response due to randomness in hydrogeological data. To the best of our knowledge, this is the first attempt in this direction.

Among the different sources of randomness, in this paper we have considered randomness of the transmissivity coefficients. We have performed a thorough analysis on how the hydraulic

range for k	N=6		N=10		N=20	
	β_k	max level	β_k	max level	β_k	max level
$1 \leq k \leq 3$	1	3	1	3	1	3
$k = 4$	3.5	0	3	1	3	1
$k = 5$	1.2	2	1.2	2	1.2	2
$k = 6$	2	1	2	1	2	1
$7 \leq k \leq 10$			3	1	3	1
$k \geq 11$					5	0

Table 3: Values of the parameter β_k and maximum level of refinement attained

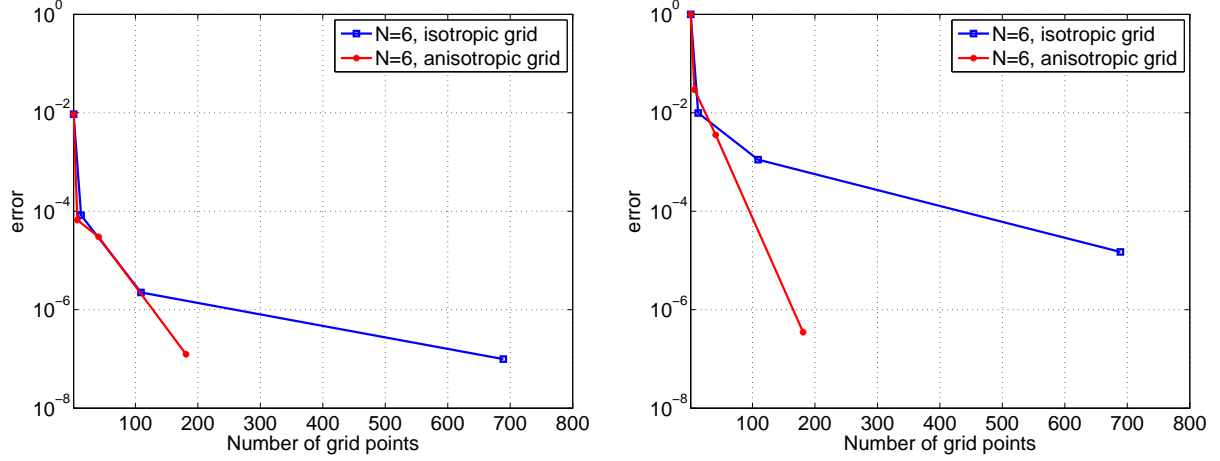


Figure 11: Test case T5: convergence curves on moments of $\phi^{(3)}$ w.r.t. number of nodes in the sparse grid. Left: mean value, right: variance.

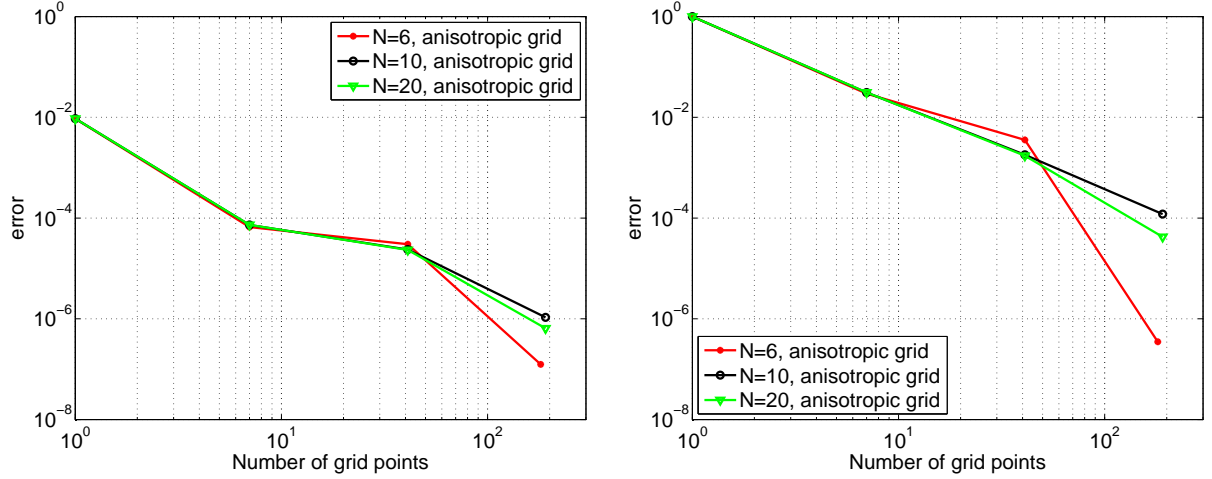


Figure 12: Test case T5: convergence curves on moments of $\phi^{(3)}$ w.r.t. number of nodes in the sparse grid. Left: mean value, right: variance.

head and certain quantities of interest derived from it depend on the stochastic variables; in particular, we have proven their analytical dependence whenever the coefficients are analytic functions of these variables (as is the case of a Karhunen-Loève expansion).

The approximate computation of the quantities of interest has been based on a stochastic collocation approach that uses suitable sparse grids in the range of the stochastic variables. This produces a non-intrusive computational method, in which the DFN flow solver is applied as a black-box.

We have tested two probability distributions (log-uniform and log-normal) within different laws of dependence of the coefficients on the stochastic variables; particular attention has been devoted to Karhunen-Loève expansions, depending on different correlation lengths. The effect of increasing the stochastic dimension has been carefully investigated.

We have monitored the accuracy in the approximation of mean value and variance for outgoing fluxes through selected fractures. We found a very fast decay of errors in the low dimensional

cases using isotropic sparse grids; comparisons with Monte Carlo results show a clear gain in efficiency for the proposed method. For increasing dimensions attained via successive truncations of Karhunen-Loève expansions, results are still good although the rates of convergence are progressively reduced. We found that resorting to suitably tuned anisotropic grids is an effective way to contrast such curse of dimensionality. In the explored range of dimensions, the resulting convergence histories are nearly independent of the dimension.

The present investigation shows the feasibility and the effectiveness of our stochastic collocation approach to UQ for DFN flow simulations. Future interesting directions of research may concern the automatic choice of the anisotropic grids, and the adaptive selection of the collocation points within the sparse grids. Exploring other sources of randomness, in particular those affecting the geometrical parameters of the network, will be a formidable challenge.

7. Acknowledgements

This research has been partially supported by the Italian research grant *PRIN 2012* 2012HBLYE4_004 “Metodologie innovative nella modellistica differenziale numerica”.

References

- [1] M. C. Cacas, E. Ledoux, G. de Marsily, B. Tillie, A. Barbreau, E. Durand, B. Feuga, P. Peaudecerf, Modeling fracture flow with a stochastic discrete fracture network: calibration and validation: 1. the flow model, *Water Resour. Res.* 26 (1990) 479–489.
- [2] S. Berrone, S. Pieraccini, S. Scialò, A PDE-constrained optimization formulation for discrete fracture network flows, *SIAM J. Sci. Comput.* 35 (2013) B487–B510.
- [3] S. Berrone, S. Pieraccini, S. Scialò, On simulations of discrete fracture network flows with an optimization-based extended finite element method, *SIAM J. Sci. Comput.* 35 (2013) A908–A935.
- [4] S. Berrone, S. Pieraccini, S. Scialò, An optimization approach for large scale simulations of discrete fracture network flows, *J. Comput. Phys.* 256 (2014) 838–853.
- [5] M. F. Benedetto, S. Berrone, S. Pieraccini, S. Scialò, The virtual element method for discrete fracture network simulations, *Computer Methods in Applied Mechanics and Engineering* 280 (2014) 135–156.
- [6] S. Berrone, S. Pieraccini, S. Scialò, F. Vicini, Scalability performances of an optimization based parallel solver for large scale dfn simulations, 2014. Politecnico di Torino, <http://porto.polito.it/2561152>.
- [7] T. Belytschko, T. Black, Elastic crack growth in finite elements with minimal remeshing, *Internat. J. Numer. Methods Engrg.* 45 (1999) 601–620.
- [8] C. Daux, N. Mões, J. Dolbow, N. Sukumar, T. Belytschko, Arbitrary branched and intersecting cracks with the extended finite element method, *Internat. J. Numer. Methods Engrg.* 48 (2000) 1741–1760.
- [9] T. Belytschko, N. Mões, S. Usui, C. Parimi, Arbitrary discontinuities in finite elements, *Internat. J. Numer. Methods Engrg.* 50 (2001) 993–1013.

- [10] W. S. Dershowitz, H. H. Einstein, Characterizing rock joint geometry with joint system models, *Rock Mechanics and Rock Engineering* 1 (1988) 21–51.
- [11] L. Beirão da Veiga, F. Brezzi, A. Cangiani, G. Manzini, L. D. Marini, A. Russo, Basic principles of virtual element methods, *Math. Models Methods Appl. Sci.* 23 (2013) 199–214.
- [12] L. Beirão da Veiga, F. Brezzi, L. D. Marini, A. Russo, The hitchhiker’s guide to the virtual element method, *Mathematical Models and Methods in Applied Sciences* 24 (2014) 1541–1573.
- [13] M. Loève, *Probability theory. I*, Springer-Verlag, New York-Heidelberg, fourth edition, 1977. Graduate Texts in Mathematics, Vol. 45.
- [14] D. Xiu, G. E. Karniadakis, The Wiener-Askey polynomial chaos for stochastic differential equations, *SIAM J. Sci. Comput.* 24 (2002) 619–644.
- [15] L. Tamellini, Polynomial approximation of PDEs with stochastic coefficients, Ph.D. thesis, Politecnico di Milano, 2012.
- [16] R. G. Ghanem, P. D. Spanos, *Stochastic finite elements: a spectral approach*, Springer-Verlag, New York, 1991.
- [17] O. P. Le Maître, O. M. Knio, *Spectral methods for uncertainty quantification. With applications to computational fluid dynamics*, Scientific Computation, Springer, New York, 2010.
- [18] D. Xiu, J. S. Hesthaven, High-order collocation methods for differential equations with random inputs, *SIAM J. Sci. Comput.* 27 (2005) 1118–1139 (electronic).
- [19] I. Babuška, F. Nobile, R. Tempone, A stochastic collocation method for elliptic partial differential equations with random input data, *SIAM J. Numer. Anal.* 45 (2007) 1005–1034.
- [20] F. Nobile, R. Tempone, C. G. Webster, A sparse grid stochastic collocation method for partial differential equations with random input data, *SIAM J. Numer. Anal.* 46 (2008) 2309–2345.
- [21] S. Smolyak, Quadrature and interpolation formulas for tensor products of certain classes of functions,, *Dokl. Akad. Nauk* 4 (1963) 240–243.
- [22] H.-J. Bungartz, M. Griebel, Sparse grids, *Acta Numer.* 13 (2004) 147–269.
- [23] T. N. L. Patterson, The optimum addition of points to quadrature formulae, *Math. Comp.* 22 (1968) 847–856.
- [24] L. N. Trefethen, Is Gauss quadrature better than Clenshaw-Curtis?, *SIAM Rev.* 50 (2008) 67–87.
- [25] A. Genz, B. D. Keister, Fully symmetric interpolatory rules for multiple integrals over infinite regions with Gaussian weight, *J. Comput. Appl. Math.* 71 (1996) 299–309.

- [26] F. Nobile, R. Tempone, C. G. Webster, An anisotropic sparse grid stochastic collocation method for partial differential equations with random input data, *SIAM J. Numer. Anal.* 46 (2008) 2411–2442.
- [27] J. Bäck, R. Tempone, F. Nobile, L. Tamellini, On the optimal polynomial approximation of stochastic PDEs by Galerkin and collocation methods., *Math. Models Methods Appl. Sci.* 22 (2012) 1250033.
- [28] P. R. Conrad, Y. M. Marzouk, Adaptive Smolyak pseudospectral approximations, *SIAM J. Sci. Comput.* 35 (2013) A2643–A2670.
- [29] J. Bäck, F. Nobile, L. Tamellini, R. Tempone, Stochastic spectral Galerkin and collocation methods for PDEs with random coefficients: a numerical comparison, in: J. S. Hesthaven, E. Ronquist (Eds.), *Spectral and High Order Methods for Partial Differential Equations*, Lecture notes in computational science and engineering 76, Springer, 2011, pp. 43–62.
- [30] P. Grisvard, Elliptic problems in nonsmooth domains, volume 24 of *Monographs and Studies in Mathematics*, Pitman (Advanced Publishing Program), Boston, MA, 1985.
- [31] G. Monegato, Stieltjes polynomials and related quadrature rules, *SIAM Review* 24 (1982) 137–158.
- [32] A. Klimke, B. Wohlmuth, Algorithm 847: spinterp: Piecewise multilinear hierarchical sparse grid interpolation in MATLAB, *ACM Transactions on Mathematical Software* 31 (2005).
- [33] A. Klimke, Sparse Grid Interpolation Toolbox – User’s Guide, Technical Report IANS report 2007/017, University of Stuttgart, 2007.
- [34] F. Nobile, L. Tamellini, Sparse grids Matlab kit, <http://csqi.epfl.ch/>, 2014.